Manuscript Number: amt-2016-189
Manuscript Type: research article
Title: Tropospheric temperature retrievals using nonlinear calibration functions in the pure rotational Raman lidar technique

First of all, we want to thank both Reviewers for their valuable criticism, comments, and suggestions which allow to improve our manuscript.

Point-by-point response to Referee 1

Comment: … However they are some weaknesses in the computation of uncertainties developed in Appendices A0 to A3 that makes the paper unpublishable in its present state and I recommend a major revision. The reasons for this recommendation are explained below. The Formula (A2) giving the uncertainty on the ratio Q between the two Raman lidar channels is not correct. As the signals in the two channels are independent of each other, the uncertainties should not be summed linearly but quadratically. The derivation of ΔT using Formulas (A3) to (A8) is therefore also not correct. Surprisingly the Formula A9 giving the uncertainty on $\Delta T/T$ is correct but I don't understand how it is possible to derive it from (A8). As a consequence there is an inconsistency in the experimental results on ΔT and $\Delta T/T$ presented on Figures 6 to 10 and 12 to 14. The ratio between ΔT and $\Delta T/T$ should be equal to the temperature T that varies between 270 K and 205 K in the altitude range covered by the lidar. The ratio on the Figures seems to be more in the order of 120K, with for instance $\Delta T/T$ =0.005 and ΔT =0.6 K. The same mistake exists also in Appendices A1 to A3.

Our response: We agree with Referee's notes regarding the mentioned formulas and Appendices. We have revised and rewritten all Appendices (A and A0–A4), and corrected equations, figures, and the Supplement data. See, please, the corrected Appendices in the list of corrections or in the revised blue-colored manuscript below.

Comment: Concerning the experimental results, the estimation of the temperature difference with the reference data CPAC is not affected by the uncertainty computation and can be considered as valid. It is clear that a nonlinear curve gives globally better results than the linear curve. It is especially true in the lower part of the atmosphere. However it is not so clear that it improves also the results above 8 km. In some cases the linear curve gives better results that the nonlinear ones, for instance at 9 km.

Response: The linear (black) curve is better than nonlinear ones (colored) only at one point (9 km). This is a random result due to a small number of the "reference" CPAC points. As seen from the comparative analysis of the difference $|T_{\mathrm{CPAC}} - T|$ between temperature values retrieved from the CPACs and IMCES lidar data in Figure 1 (below), three calibration functions (red, green, and blue curves) retrieve the temperature better than the linear one at an altitude of ~11.5 km.

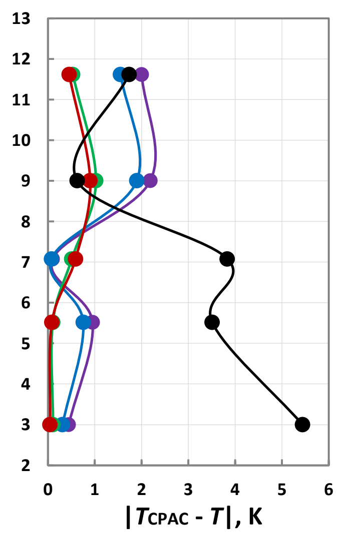

Figure 1. Difference $|T_{\mathrm{CPAC}} - T|$ between temperature values retrieved from the CPACs and IMCES lidar data.

Comment: Do the authors have an explanation for that and is it necessary to apply a nonlinear curve in the full tropospheric range or only in the lower part?

Response: As we have experimentally shown in Figure 1 and in our previous Optics Express paper via simulation (Gerasimov and Zuev, 2016), the considered nonlinear calibration functions are preferable for temperature retrievals in the full tropospheric range.

Gerasimov, V. V. and Zuev, V. V.: Analytical calibration functions for the pure rotational Raman lidar technique, Opt. Express, 24, 5136–5151, 2016.

Point-by-point response to Referee 2

Comment: … The general statement that the "commonly used calibration function" would yield significant errors of 1 K is wrong (abstract, line 14). The bias of current state-of-the-art RRL systems is only < 0.5 K (see Wulfmeyer et al. 2015 for a recent review).

Our response: We cannot completely agree with this Referee's note concerning the error of ±1 K. We were based on theoretical (simulation) error estimations presented by Behrendt (2005). According to Fig. 10.3 (Behrendt, 2005, page 288), the error can exceed a value of 2 K at an air temperature of ~300 K. Nevertheless, we removed this statement from the Abstract.

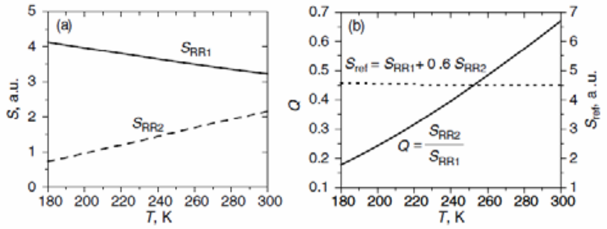

Fig. 10.2. (a) Typical intensities of the two pure-rotational Raman signals S_{RR1} and S_{RR2} as a function of temperature T [48]. (b) Signal ratio Q from which the atmospheric temperature is derived. S_{ref} can be used as a temperature-independent Raman reference signal for measuring extinction and backscatter coefficients of aerosols and cloud particles [47].

state-of-the-art radiosondes are accurate within tenths of a K provided the radiosonde itself has been accurately calibrated. Of course, the reference data used for the calibration should be taken as close in space and time as possible to the atmospheric column sensed by the lidar. How often an RR lidar systems needs to be recalibrated depends on the individual system. Provided that rugged mounts are used and the alignment of the lidar is not changed intentionally, the calibration of today's state-of-art systems remains virtually unchanged and only long-term degradations of the optical components may require recalibrations on a longer time scale.

For systems that detect only one RR line in each of the two RR channels Eq. (10.25) takes the simple form

$$Q(T) = \exp(a - b/T), \qquad (10.26)$$

where the parameters a and b are both positive if $J(S_{RR2}) > J(S_{RR1})$. b is simply the difference of the rotational Raman energies of the extracted lines divided by k, and a is the logarithm of the ratio of all factors except the exponential term in Eq. (10.20). It is straightforward to use Eq. (10.26) also for systems with several lines in each of the RR signals [42]. But the obvious inversion of Eq. (10.26) which gives

$$T = \frac{b}{a - \ln Q} \qquad (10.27)$$

then turns out to yield significant measurement errors, well in excess of 1 K (cf. Fig. 10.3) when measurements are made over an extended

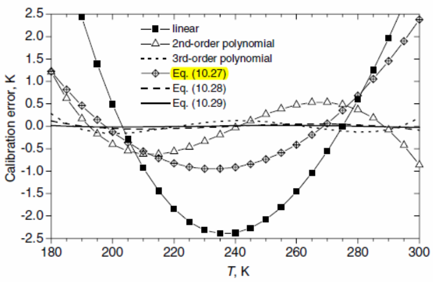

Fig. 10.3. Errors made with different calibration functions for rotational Raman temperature lidar.

range of temperatures. As the errors behave nearly as a second-order-polynomial function of temperature, it has been proposed to minimize calibration errors by a second calibration with such a second-order polynomial [43, 62], leading to a calibration function of the form

$$T = \frac{b}{a - \ln Q} + c\left(\frac{b}{a - \ln Q}\right)^2 + d \qquad (10.28)$$

with the additional calibration constants c and d.

An even better calibration function, however, is found in the approach

$$Q = \exp\left(\frac{a'}{T^2} + \frac{b'}{T} + c'\right) \Longleftrightarrow T = \frac{-2a'}{b' \pm \sqrt{b'^2 - 4a'(c' - \ln Q)}}, \qquad (10.29)$$

which extends Eq. (10.26) to a second-order term in T and needs only three calibration constants a', b', c'. Fitting, as an example, the curve $T(Q)$ shown in Fig. 10.2 with the different calibration functions, one gets the calibration errors shown in Fig. 10.3. The performances of polynomial calibration functions are also given for comparison. The single-line approach of Eq. (10.27) results here in errors of ~±1 K for temperatures between 180 and 285 K, which is better than a linear calibration function. However, this relation is not generally valid [63]. For three calibration constants, Eq. (10.29) is superior to the second-order polynomial and even better than the third-order polynomial and the approach of Eq. (10.28), which both require four calibration constants. For Eq. (10.29), the temperature derived from the data with that

Instead of

"The commonly used calibration function linear in reciprocal temperature ignores the broadening of individual atmospheric N_2 and O_2 PRR lines and, at the same time, yields significant errors (±1 K) in temperature retrievals."

we wrote

"...The commonly used calibration function (linear in reciprocal temperature $1/T$ with two calibration coefficients) ignores all types of broadening of individual PRR lines of atmospheric N_2 and O_2 molecules."
[**Page 1, lines 13–14, revised manuscript**]

Comment: … While the first and second author of this manuscript have recently published simulations on this topic, the goal of this manuscript is to show experimental comparisons between RRL temperature data obtained with different calibration functions and "reference" data. Unfortunately, the study lacks such suitable reference data. The RRL measurements were taken at a site for which unfortunately no local radiosonde ascents were available. The closest radiosonde launching sites are more than 250 km away (see section 4.2). But this is clearly much too far for suitable comparisons. In addition, the authors use data of constant pressure altitude charts with low vertical resolution to overcome the large distances to the radiosonde sites but also these are certainly related to too large uncertainties for being used as reference data for investigating the small differences between the calibration functions. Also with a perfect calibration function, one could not "force" uncorrelated temperature data to agree.

Response: We agree with this Referee's note about "reference" data. However, the temperature points retrieved using available constant pressure altitude charts (CPACs) with the temperature accuracy of 0.5 K and the vertical accuracy of 20 m allow to make the comparative analysis of temperature uncertainties, yielded by using different calibration functions, and determine the best-suited function for our lidar system. So, we added two explaining sentences at the end of Sect. 4.2.

Instead of

"…the University of Wyoming (Novosibirsk and Kolpashevo station numbers are 29634 and 29231, respectively)."

we wrote

"...the University of Wyoming (Novosibirsk and Kolpashevo station numbers are 29634 and 29231, respectively). It is clear that the CPAC points are not suitable for using them as the reference points to calibrate lidars and retrieve temperature profiles with high accuracy (for this purpose the local radiosonde data are required). Nevertheless, the accuracy of these points (0.5 K, 20 m) is sufficient to make the comparative analysis of temperature uncertainties, yielded by using different calibration functions, and determine the best-suited function (among them) for our lidar system."
[**Page 8, lines 17–22, revised manuscript**]

Comment: It may be possible that the lidar system used by the authors is special and that for this system a more complicated calibration function is needed than for other RRL systems described in the literature. The calibration errors depend of the spectral characteristics of the lidar receiver, namely the widths, central wavelengths, shapes of the transmission functions as well as whether just the anti-Stokes or both branches of the pure rotational Raman spectrum are collected. I could imagine that especially the last point combined with narrow transmission bands may lead to larger calibration errors when using a too simple calibration function. Maybe this could explain why the commonly used calibration functions do not seem to work well for the RRL discussed here. More simulations for different types of RRL systems would be needed to verify this hypothesis – or, even better, collocated RRL measurements with different types of systems. Maybe this very interesting experiment could be realized in the future.

Response: We agree. That's quite possible. Despite the nonlinear calibrations functions, derived in (Gerasimov and Zuev, 2016) and applied in the current AMTD paper, represent a direct consequence of the collisional broadening of PRR lines, we do not exclude the possibility that the best-suited function can depend on the PRR lidar system. We noted that at the end of Sect. 6.

Instead of

"As the best function for temperature retrievals can depend on a lidar system (e.g., based on DGs or IFs for PRR lines extracting), it is reasonable to check all the mentioned nonlinear functions against lidar data obtained with different lidar systems to determine the best function in each specific case. As the collisional broadening of PRR lines is the largest in the atmospheric boundary layer, the nonlinear calibrations functions should be applied instead of the linear one for temperature retrievals, especially if using a coaxial lidar."

we wrote

As it was mentioned above (Sect. 4.2), the CPAC points can hardly be used as the reference data to reliably calibrate PRR lidars and retrieve accurate temperature profiles. Nevertheless, the results suggest that the best-suited calibration function for temperature retrievals can depend on the lidar system (e.g., based on DGs or IFs for PRR lines extracting), which can take into account the collisional broadening of PRR lines in varying degrees. Indeed, the calibration errors depend on the spectral characteristics of the lidar receiver such as the central wavelength, shape and width of the transmission functions, as well as whether just the anti-Stokes (IFs) or both branches of the PRR spectrum (DGs) are used to extract the PRR signals from backscattered light. Therefore, it is reasonable to check all the mentioned nonlinear functions against lidar data obtained with different lidar systems to determine the best function in each specific case." [**Page 10, lines 26–31 and Page 11, lines 1 and 2, revised manuscript**]

Comment: My suggestion is to revise the manuscript substantially and to rewrite the statements which are too general by clarifying that this study is on the data of a special/unique RRL system and comparisons with model temperature data which possess certain uncertainties. It should be made clear that the results may be used as indication (not proof) that some RRL systems may require more complicated calibration functions than the ones reported so far in the literature and that better reference data for comparisons will be useful to support this interpretation.

Response: We have deeply revised the text of our manuscript. The abstract, Sects. 4.1 and 6, and Appendix A were significantly rewritten (see, please, the list of corrections or revised blue-colored manuscript below). The results can be considered as preliminary in the absence of reliable radiosonde data, and we offer to lidar researcher to use these nonlinear functions and determine the best one in each specific case of the PRR lidar system.

Specific comments of Referee 2

Comment: Title: Maybe better “Tropospheric temperature measurements with the pure rotational Raman lidar technique using nonlinear calibration functions”. RRL does not “retrieve” the temperature; there is no first guess like in passive remote sensing.

Response: Thank you for your suggestion. Yes, we know that calibration function retrieve the temperature, not a PRR lidar. To make the title more clear, we slightly rewrote it.

Instead of
“Tropospheric temperature retrievals using nonlinear calibration functions in the pure rotational Raman lidar technique”

we wrote
“Tropospheric temperature retrievals using nonlinear calibration functions in the frame of the pure rotational Raman lidar technique.”
[**Page 1, lines 1 and 2, revised manuscript**]

Comment: Abstract, line 13 ff: This general statement is (fortunately) wrong. The calibration functions used so far lead (for all systems discussed in the literature) much smaller errors due to the calibration function itself. In addition, the error depends on the temperature range of the calibration. See general comments above. Please rewrite.

Response: It was already discussed above.

Comment: Abstract, line 15 ff: The statement that “collisional broadening … cannot be neglected (for) tropospheric temperature measurements” is too general. Again, this depends on the individual characteristics of the RRL system and the temperature range etc. Please omit or clarify.

Response: Rewritten.

Instead of
“However, the collisional (or pressure) broadening of N_2 and O_2 PRR lines dominates over other types of broadening in the troposphere, and therefore, cannot be neglected during tropospheric temperature measurements.”

we wrote
“However, the collisional (pressure) broadening dominates over other types of broadening of PRR lines in the troposphere and can differently affect the accuracy of tropospheric temperature measurements depending on the PRR lidar system.”
[**Page 1, lines 13–15, revised manuscript**]

Comment: Page 2, line 4 and section 4.1: I do not like the term “smoothing” because it could include different types of filters which are not preferable and not meant. I suggest simply writing “averaging in time and range”.

Response: The term “smoothing” was substituted by the term “averaging” throughout the manuscript.

Comment: Further averaging of the ratio should be avoided. It only complicates the effective weighting function of the resulting data while the averaging of the raw data should anyhow be made with sufficiently large windows in order to avoid too large noise errors when taking the ratio.

Response: We have to disagree with this suggestion. In some cases, the second-order averaging of raw data (or/and their ratio) is required and more preferable than the first-order one (see, e.g., El'nikov et al., 2000). Here we applied the second-order averaging of raw data to reduce signal statistical fluctuations (see Sect. 4.1, Appendix A, and examples below). Both the uncertainties $\Delta\overline{T}$ and $(\overline{\Delta T}/T)$ decrease by $\sqrt{n}=\sqrt{11}$ times, when using additional slight smoothing for our lidar data. For example:

(1 April 2015, Eq. 13)

Without additional slight smoothing

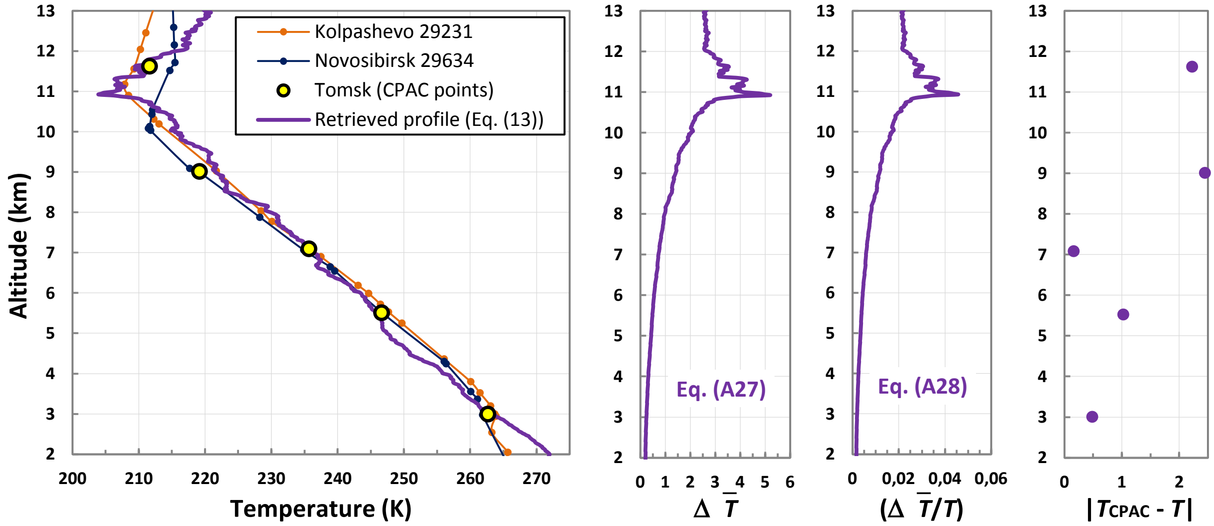

With additional slight smoothing

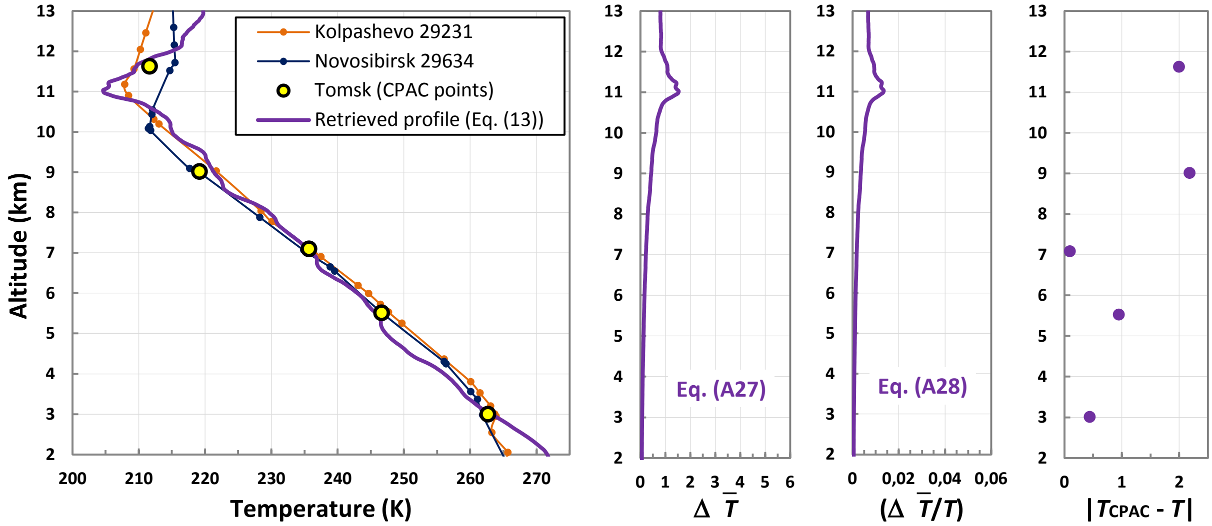

(1 April 2015, Eq. 15)

Without additional slight smoothing

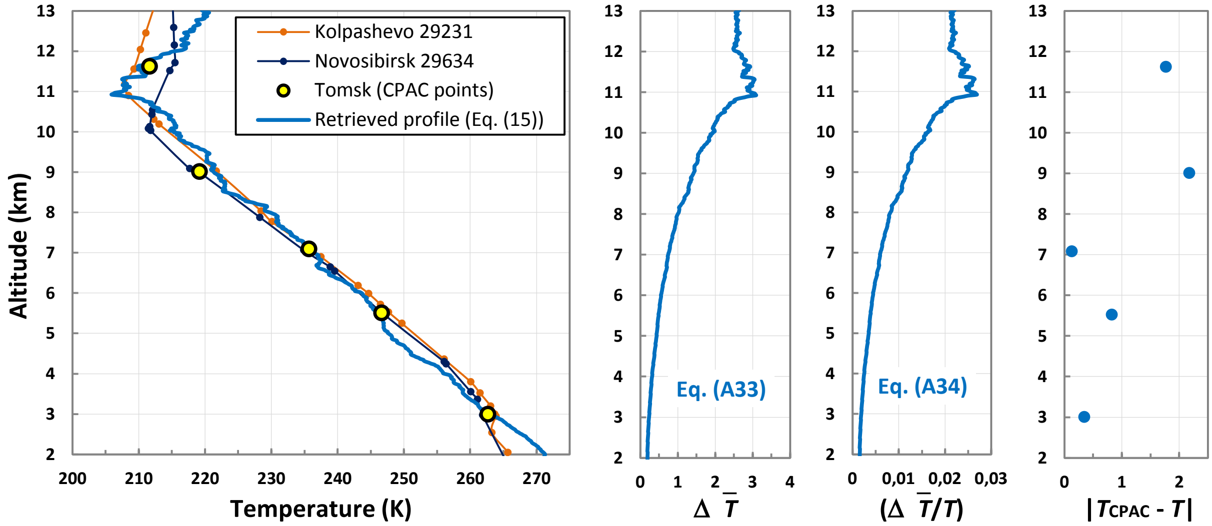

With additional slight smoothing

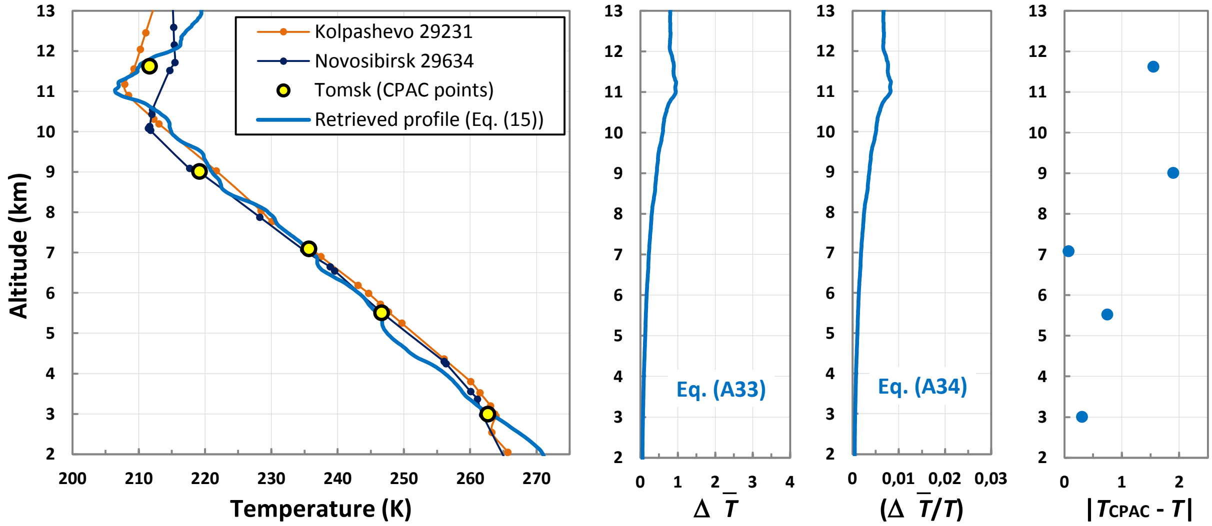

(2 October 2014, Eq. 13)

Without additional slight smoothing

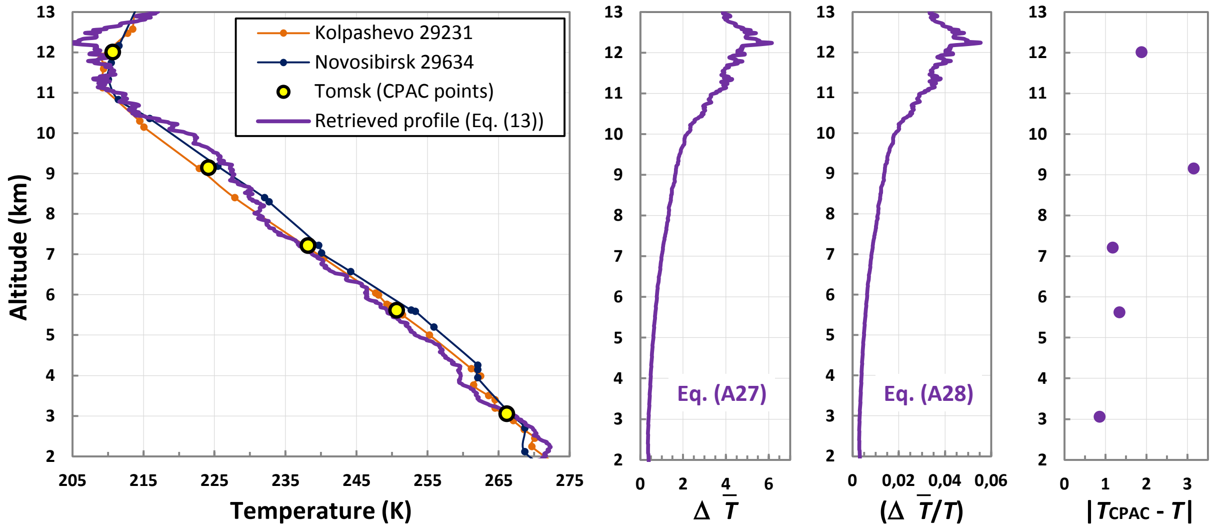

With additional slight smoothing

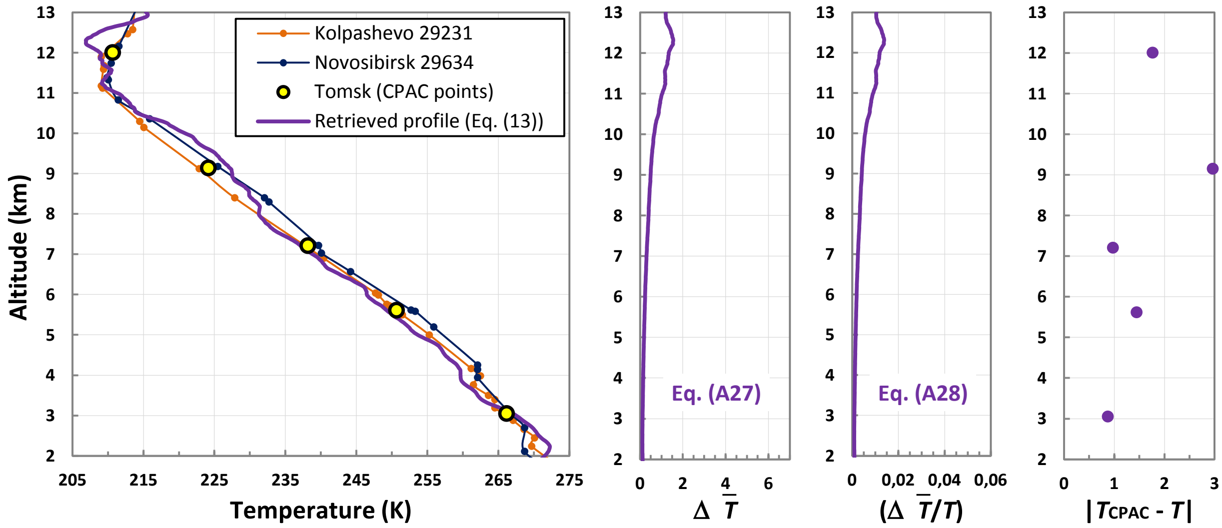

(2 October 2014, Eq. 15)

Without additional slight smoothing

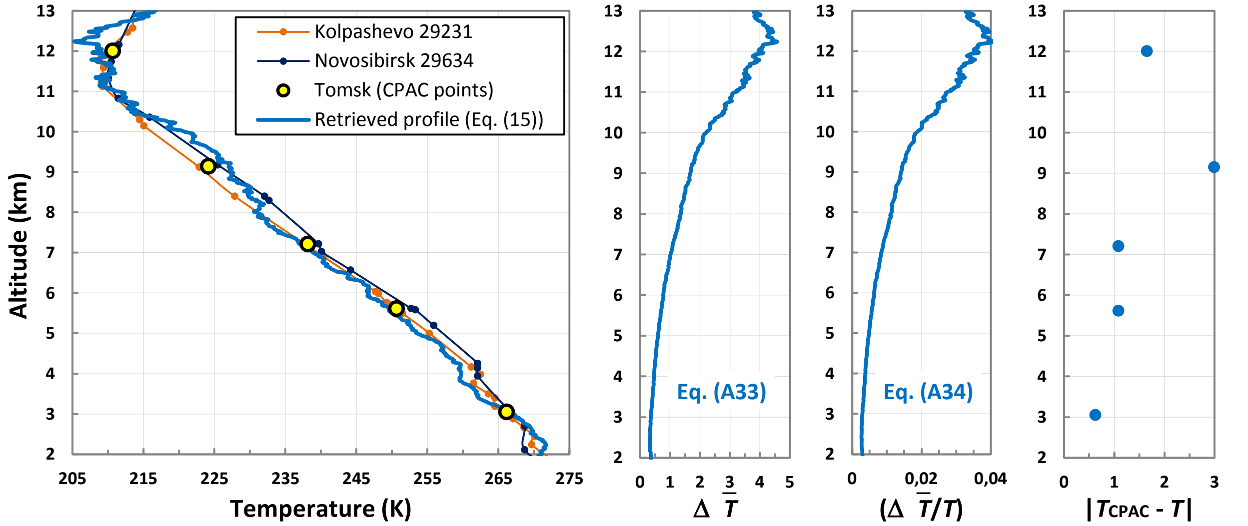

With additional slight smoothing

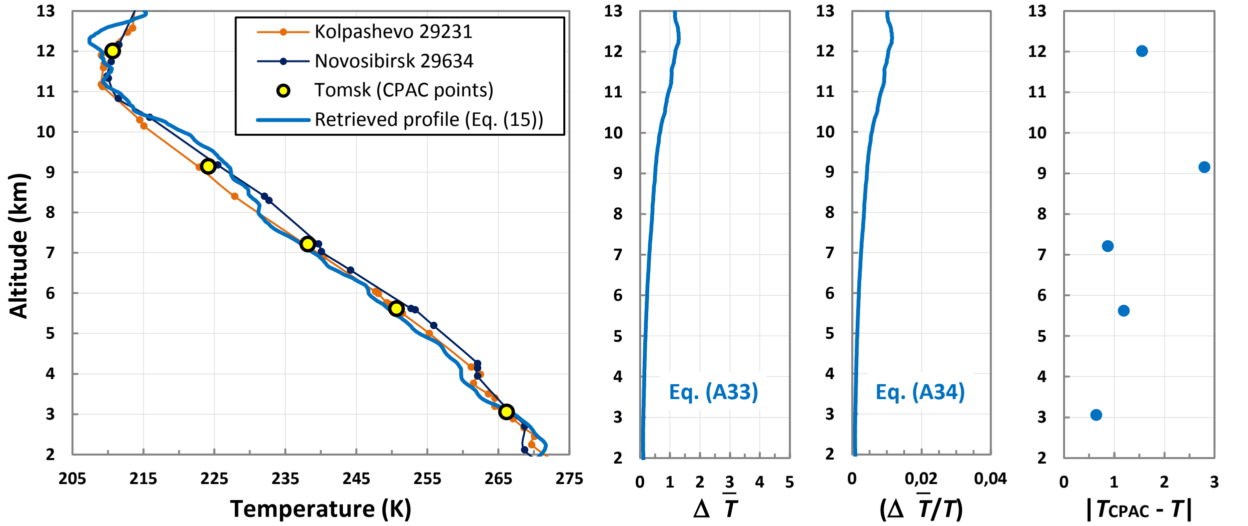

Definitely, there is no need to additionally smooth lidar data in case of usage of a high power laser as a lidar transmitter (see, e.g., Jia and Yi, 2014), but in our case, such a smoothing is required.

Comment: Equations 1, 2, 3 and related text: The instrumental efficiency which is different for different lines is not yet included here but should be included. Otherwise, "calibration" does not make sense.

Response: We have to disagree again. According to Arshinov et al. (1983, page 2985), an approximation (calibration) function is required for Eq. (3), even if the instrumental efficiency is omitted. This is due to the fact that Eq. (3) already has a complicated temperature dependence, cannot be expressed as a simple function of *T*, and therefore, cannot be used for temperature retrievals. Only Eq. (2) does not require a calibration.

Comment: Section 4.1: What is the resolution of the raw data? As said above, further averaging of the ratio is not preferable. What is otherwise the effective weighting function of the double-averaged data?

Response: This information now can be found in Sect. 4.1 and Appendix A (see Eqs. A13–A17).

Comment: Section 4.3: It should be made clear that the CPAC data are not a reference. Thus large differences between the RRL and CPAC data are not necessarily due to problems with the calibration function. I suggest that you show in addition the calibration plots (T_CPAC versus T_RRL with calibration function).

Response: Figures 10 and 15 were added to the revised manuscript (T_CPAC versus T_RRL with calibration function).

Comment: Appendix A: The propagation of the Poisson errors have already been discussed extensively in the literature for the calibration functions used so far – also including the contribution of the background signal which is missing here. Thus, these parts should be deleted here. Instead, references to the existing literature should be given which are currently missing.

Response: We agree. As it was mentioned above, we significantly revised Appendix A.

Comment: Figure 1: Please explain also the red and blue curves and identify the laser wavelength.

Response: Done.

Comment: Figure 2: Should be deleted as this photo does not explain any technical details. Figure 3 is enough and much better I think.

Response: Figure 2 was removed from the manuscript.

Comment: Figure 3: Which PMT is used for which signal?

Response: The PMTs Hamamatsu R7207-01 are used both for elastic and two inelastic (PRR) channels. This information is in Table 1.

Arshinov, Y. F., Bobrovnikov, S. M., Zuev, V. E., and Mitev, V. M.: Atmospheric temperature measurements using a pure rotational Raman lidar, Appl. Optics, 22, 2984–2990, 1983.

Behrendt, A.: Temperature measurements with lidar, in: Lidar: Range-Resolved Optical Remote Sensing of the Atmosphere, edited by: Weitkamp, C., Springer, New York, 2005.

Gerasimov, V. V. and Zuev, V. V.: Analytical calibration functions for the pure rotational Raman lidar technique, Opt. Express, 24, 5136–5151, 2016.

El'nikov, A. V., Zuev, V. V., and Bondarenko, S. L.: Retrieving the profiles of stratospheric ozone from lidar sensing data, Atm. and Oceanic Optics, 13, 1029–1034, 2000.

Jia, J. and Yi, F.: Atmospheric temperature measurements at altitudes of 5–30 km with a double-grating-based pure rotational Raman lidar, Appl. Optics, 53, 5330–5343, 2014.

List of corrections

Figure 2 was removed from the old version of the manuscript, whereas Figs. 10 and 15 were added to the revised manuscript.

Two references were added to the text and list of references:

Li, Y.-J., Song, S.-L., Li, F.-Q., Cheng X.-W., Chen, Z.-W., Liu, L.-M., Yang, Y., and Gong, S.-S.: High-precision measurements of lower atmospheric temperature based on pure rotational Raman lidar, Chinese J. Geophys., 58, 2294–2305, 2015.

Wulfmeyer, V., Hardesty, R. M., Turner, D. D., Behrendt, A., Cadeddu, M. P., Di Girolamo, P., Schlüssel, P., Van Baelen, J., and Zus, F.: A review of the remote sensing of lower tropospheric thermodynamic profiles and its indispensable role for the understanding and the simulation of water and energy cycles. Rev. Geophys., 53, 819–895, 2015.

The term “smoothing” was substituted by the term “averaging” throughout the manuscript

Page 1 (Title)

Instead of
“Tropospheric temperature retrievals using nonlinear calibration functions in the pure rotational Raman lidar technique”

we wrote
“Tropospheric temperature retrievals using nonlinear calibration functions in the frame of the pure rotational Raman lidar technique.”
[**Page 1, lines 1 and 2, revised manuscript**]

Page 1 (Abstract)

Instead of

"Among lidar techniques for temperature measurements, the pure rotational Raman (PRR) technique is the best-suited for tropospheric and lower stratospheric temperature profiling. Calibration functions play a key role in the temperature retrieval algorithm from backscattered signals using the PRR lidar technique. The temperature retrieval accuracy and number of calibration coefficients depend on the selected calibration function. The commonly used calibration function linear in reciprocal temperature ignores the broadening of individual atmospheric N_2 and O_2 PRR lines and, at the same time, yields significant errors (±1 K) in temperature retrievals. However, the collisional (or pressure) broadening of N_2 and O_2 PRR lines dominates over other types of broadening in the troposphere, and therefore, cannot be neglected during tropospheric temperature measurements. Gerasimov and Zuev (2016) derived mathematically a calibration function in the general analytical form that takes into account the collisional broadening of all N_2 and O_2 PRR lines. Nevertheless, this general calibration function represents an infinite series and cannot be directly used in the temperature retrieval algorithm. Therefore, four simplest nonlinear special cases (having three calibration coefficients) of the function, two of which have not been suggested before, were considered and analyzed, and the best calibration function among them was determined via simulation. In this paper, we apply these special cases to real lidar remote sensing data, because all the functions take into account the collisional PRR lines broadening in varying degrees. The best-suited calibration function for tropospheric temperature retrievals is determined from the comparative analysis of temperature uncertainties yielded by using these functions..."

we wrote

"Among lidar techniques, the pure rotational Raman (PRR) technique is the best-suited for tropospheric and lower stratospheric temperature measurements. Calibration functions are required for the PRR technique to retrieve temperature profiles from lidar remote sensing data. Both temperature retrieval accuracy and number of calibration coefficients depend on the selected function. The commonly used calibration function (linear in reciprocal temperature $1/T$ with two calibration coefficients) ignores all types of broadening of individual PRR lines of atmospheric N_2 and O_2 molecules. However, the collisional (pressure) broadening dominates over other types of broadening of PRR lines in the troposphere and can differently affect the accuracy of tropospheric temperature measurements depending on the PRR lidar system. We recently derived the calibration function in the general analytical form that takes into account the collisional broadening of all N_2 and O_2 PRR lines (Gerasimov and Zuev, 2016). This general calibration function represents an infinite series and, therefore, cannot be directly used in the temperature retrieval algorithm. For this reason, its four simplest special cases (calibration functions nonlinear in $1/T$ with three calibration coefficients), two of which have not been suggested before, were considered and analyzed. All the special cases take the collisional PRR lines broadening into account in varying degrees and the best function among them was determined via simulation. In this paper, we use the special cases to retrieve tropospheric temperature from real PRR lidar data. The calibration function best-suited for tropospheric temperature retrievals is determined from the comparative analysis of temperature uncertainties yielded by using these functions…"

[**Page 1, lines 9–23, revised manuscript**]

Page 2 (1 Introduction)

Instead of

"The retrieval algorithm of a vertical temperature profile of the lower atmosphere from pure rotational Raman (PRR) raw lidar signals is known to consist of four main steps:

1. Smoothing PRR raw lidar signals and/or their ratio;
2. Lidar calibration, i.e. determination of the lidar calibration function coefficients by applying the least square method to the reference radiosonde (or model) data and previously smoothed lidar data;
3. Temperature profile retrieval by using the temperature retrieval function derived from the calibration function;
4. Estimation of the temperature retrieval absolute and relative uncertainties.

The PRR lidar technique suggested by Cooney (1972) is based on the temperature dependence of individual lines intensity of atmospheric N_2 and O_2 molecules PRR spectra."

we wrote

"The pure rotational Raman (PRR) technique is known to be the best-suited for lower atmosphere temperature measurements (Wulfmeyer et al., 2015). The retrieval algorithm of vertical temperature profiles of the troposphere and lower stratosphere from PRR lidar raw signals consists of four main steps:

1. PRR lidar raw data averaging to improve the signal-to-noise ratio and decrease the statistical uncertainties;
2. Lidar calibration, i.e. determination of the lidar calibration function coefficients by applying, e.g., the least square method to the reference radiosonde (or model) data and previously averaged lidar data;
3. Temperature profile retrieval by using the temperature retrieval function derived from the selected calibration function;

4. Estimation of the absolute and relative uncertainties of the temperature retrieval, and calculation of the difference between the reference temperature (radiosonde, model) and temperature retrieved from lidar data.

The PRR lidar technique suggested by Cooney (1972) is based on the temperature dependence of individual lines intensity of atmospheric N_2 and O_2 PRR spectra."

[**Page 2, lines 2–13, revised manuscript**]

Page 4 (1 Introduction)

Instead of

"Taking Eqs. (5) and (6) into account, the ratio of photocounts from two spectrally close bands involving several N_2 and O_2 PRR lines with J_{low} and J_{high} becomes (Newsom et al., 2012; Newsom et al., 2013)

$$Q(T,z) = \frac{N_{\text{low}}(T,z)}{N_{\text{high}}(T,z)} = \frac{G_{\text{low}}(z)}{G_{\text{high}}(z)} \exp\left(\sum_{n=-\infty}^{\infty} B_n T^{\frac{n}{2}} \right) = O(z) \exp\left(\sum_{n=-\infty}^{\infty} B_n T^{\frac{n}{2}} \right), \tag{7}$$

where B_n are the calibration coefficients; $O(z)$ is the laser-beam receiver-field-of-view overlap function."

we wrote

"Taking Eqs. (5) and (6) into account, the ratio of the background-subtracted photocounts N_{L} and N_{H} from two spectrally close bands involving several N_2 and O_2 PRR lines with J_{low} and J_{high} becomes (Newsom et al., 2012; Newsom et al., 2013)

$$Q(T,z) = \frac{N_{\text{L}}(T,z)}{N_{\text{H}}(T,z)} = \frac{G_{\text{L}}(z)}{G_{\text{H}}(z)} \exp\left(\sum_{n=-\infty}^{\infty} B_n T^{\frac{n}{2}} \right) = O(z) \exp\left(\sum_{n=-\infty}^{\infty} B_n T^{\frac{n}{2}} \right), \tag{7}$$

where B_n are the calibration coefficients; $O(z) = G_{\text{L}}(z)/G_{\text{H}}(z)$ is the laser-beam receiver-field-of-view overlap function."

[**Page 4, lines 14–18, revised manuscript**]

Page 5 (1 Introduction)

Instead of

"In this paper, we apply these calibration functions to real lidar remote sensing data, because all the functions take into account the collisional PRR lines broadening in varying degrees, and determine the best-suited function for tropospheric temperature retrievals."

we wrote

"In this paper, we apply these calibration functions to real lidar remote sensing data. The calibration function best-suited for tropospheric temperature retrievals (for our PRR lidar system) is determined from the comparative analysis of temperature uncertainties yielded by using these functions."

[**Page 4, line 27 and Page 5, lines 1 and 2, revised manuscript**]

Page 5 (2 Special cases of the general calibration function)

Instead of

"Here we consider the linear (i.e. two-coefficient) and four simplest nonlinear (three-coefficient) in reciprocal temperature calibration functions and their corresponding temperature retrieval functions."

we wrote

"Here we consider the linear and four simplest nonlinear (in reciprocal temperature $1/T$) calibration functions and their corresponding temperature retrieval functions."

[**Page 5, lines 8 and 9, revised manuscript**]

Page 6 (2 Special cases of the general calibration function)

The following explaining sentences were added to the manuscript:

"All the nonlinear calibration (or temperature retrieval) functions considered here take into account in varying degrees the collisional PRR lines broadening."

[**Page 6, lines 19 and 20, revised manuscript**]

Pages 7 and 8 (4.1 Raw lidar data averaging)

Instead of

"In order to improve the signal-to-noise ratio, the raw lidar data (photocounts N_{L} and N_{H} detected by PMTs in the DGM channels) should be smoothed. We tested more than dozens of different data-smoothing methods including the equal-sized and variable sliding-window smoothing ones presented in various papers (Behrendt and Reichardt, 2000; Behrendt et al., 2002; Alpers et al., 2004; Di Girolamo et al., 2004; Radlach et al., 2008; Radlach, 2009; Jia and Yi, 2014). The optimal data-smoothing method for our lidar system was the following. The IMCES lidar raw data were vertically smoothed with a variable sliding average window (Appendix A). Having the initial 48m length (Δz = 24 m, k = 1, and n = 3 in Eq. A10) in the lidar to 240m altitude range, the variable sliding window was increased above and below by 24 m for every 240 m increase in altitude (see Fig. 4a). Note that similar lidar-data-smoothing procedure was used, e.g., in (Lee III, 2013). Due to low power of the IMCES lidar laser, the smoothed signals ratio $Q = \overline{N}_{\mathrm{L}} / \overline{N}_{\mathrm{H}}$ was additionally slightly smoothed using the equal-sized sliding window (k = 5, and n = 11 in Eq. A10) to reduce signal statistical fluctuations, as shown in Fig. 4b (see also the Supplement). For any other lidar system, the best data-smoothing method can differ from the method we used."

we wrote

"In order to improve the signal-to-noise ratio, raw lidar data (background-subtracted photocounts N_{L} and N_{H} detected by PMTs in the DGM channels) should be averaged. We tested more than dozens of different data-averaging methods including the equal-sized and variable sliding-window averaging ones presented in various papers (Behrendt and Reichardt, 2000; Behrendt et al., 2002; Alpers et al., 2004; Di Girolamo et al., 2004; Radlach et al., 2008; Radlach, 2009; Jia and Yi, 2014). The optimal data-averaging method for our lidar system is the following. The IMCES lidar raw data with vertical resolution of Δz = 24 m are averaged with a variable sliding average window (Appendix A). Having an initial size of $n = 2k + 1 = 3$ (k = 1), the sliding window is increased by one point on either side of the central point for every ten data points. Otherwise, starting with an initial length of $\Delta\overline{z} = n\Delta z = 72$ m in the lidar to 240m altitude range, the sliding window is increased above and below by 24 m for every 240m increase in altitude (see Fig. 3a). For example, the sliding window size and length (or averaged data resolution) are of n = 27 (k = 13) and $\Delta\overline{z} = 648$ m at an altitude of 3 km, and n = 85 (k = 42) and $\Delta\overline{z} = 2040$ m at an altitude of 10 km, respectively. Note that similar lidar-data-averaging procedure was used, e.g., in (Lee III, 2013). Due to low power of the IMCES lidar laser, the ratio of single-averaged signals (i.e. $Q = \overline{N}_{\mathrm{L}} / \overline{N}_{\mathrm{H}}$) was additionally slightly averaged with a small equal-sized sliding window (l = 5, and m = 11 in Eq. A7) to reduce signal statistical fluctuations (Fig. 3b, see also the Supplement). For example, the double-averaged data resolution becomes $\Delta\overline{\overline{z}} = [2(k+l)+1]\Delta z = 2280$ m (k = 42, l = 5) at an altitude of 10 km, but both absolute and relative statistical uncertainties additionally decrease by $\sqrt{m} = \sqrt{11}$ times (Appendix A). For any other lidar system, the optimal data-averaging method can differ from the method we used."

Page 8 (4.2 Reference temperature points for the lidar calibration)

Instead of

"The radiosondes data can be found on the webpage http://weather.uwyo.edu/upperair/sounding.html?region=np of the University of Wyoming (Novosibirsk and Kolpashevo station numbers are 29634 and 29231, respectively)."

we wrote

"The radiosondes data are presented only for comparison and can be found on the webpage http://weather.uwyo.edu/upperair/sounding.html?region=np of the University of Wyoming (Novosibirsk and Kolpashevo station numbers are 29634 and 29231, respectively). It is clear that the CPAC points are not suitable for using them as the reference points to calibrate lidars and retrieve temperature profiles with high accuracy (for this purpose the local radiosonde data are required). Nevertheless, the accuracy of these points (0.5 K, 20 m) is sufficient to make the comparative analysis of temperature uncertainties, yielded by using different calibration functions, and determine the best-suited function (among them) for our lidar system."

[**Page 8, lines 16–22, revised manuscript**]

Page 9 (4.3 Temperature profiles retrieved with different calibration functions)

Instead of

"Comparing all five profiles, one can see that, despite the lowest values of both the statistical uncertainties in the 3–12km altitude region ($\Delta\overline{T}$ < 0.5 K, $(\overline{\Delta T / T})$ < 0.004) yielded by using Eq. (11), the difference $|T_{\mathrm{CPAC}} - T|$ can exceed 5.5 K (Fig. 6). For the nonlinear functions in the same altitude region, the maximum difference $|T_{\mathrm{CPAC}} - T|$ is less than 2.2 K and 1 K when using Eq. (13) and Eq. (20), respectively, as seen from Figs. 7 and 10. Similarly, for both the uncertainties we have: $\Delta\overline{T}$ < 1.5 K, $(\overline{\Delta T / T})$ < 0.013 when applying Eq. (13), and $\Delta\overline{T}$ < 0.7 K, $(\overline{\Delta T / T})$ < 0.006 for Eq. (20). Note that the tropopause is located near 11km altitude. Taking into account all three parameters $\Delta\overline{T}$, $(\overline{\Delta T / T})$, and $|T_{\mathrm{CPAC}} - T|$, we can conclude that Eqs. (13), (15), (18), and (20) retrieve the tropospheric temperature much better compared to Eq. (11). Moreover, the two best-suited functions for temperature retrievals, which yield the minimum uncertainties and $|T_{\mathrm{CPAC}} - T|$ among considered, are presented by Eqs. (18) and (20)."

we wrote

"Comparing all five profiles among themselves, one can see that, despite the lowest values of both the statistical uncertainties in the 3–12km altitude region ($\Delta\overline{\overline{T}}$ < 0.7 K, $(\overline{\overline{\Delta T / T}})$ < 0.004) yielded by using Eq. (11), the difference $|T_{\mathrm{CPAC}} - T|$ can reach ~5.5 K (Fig. 5). For the nonlinear functions in the same altitude region, the maximum difference $|T_{\mathrm{CPAC}} - T|$ is less than 2.2 and ~0.9 K when using Eq. (13) and Eq. (20), respectively, as seen in Figs. 6, 9 and 10 (see also the Supplement). Similarly, for both the uncertainties we have: $\Delta\overline{\overline{T}}$ < 2.3 K, $(\overline{\overline{\Delta T / T}})$ < 0.011 when applying Eq. (13), and $\Delta\overline{\overline{T}}$ < 1 K, $(\overline{\overline{\Delta T / T}})$ < 0.005 for Eq. (20). Note that the peaks of curves $\Delta\overline{\overline{T}}$ and $(\overline{\overline{\Delta T / T}})$ near 11km altitude in Figs. 6 and 7 are caused by the problem with square roots in Eqs. (13) and (15) described in Appendices A1 and A2. There is no such problem in case of Eqs. (18) and (20) without square roots. The tropopause is also located near 11km altitude. Taking into account all three parameters $\Delta\overline{\overline{T}}$, $(\overline{\overline{\Delta T / T}})$, and $|T_{\mathrm{CPAC}} - T|$, we can conclude that Eqs. (13), (15), (18), and (20) retrieve the tropospheric temperature much better compared to Eq. (11). Moreover, the functions expressed by Eqs. (18) and (20) yield the smallest uncertainties and $|T_{\mathrm{CPAC}} - T|$ values among considered nonlinear functions, and therefore, they are the best-suited for tropospheric temperature retrievals with the IMCES PRR lidar."

[**Page 9, lines 3–14, revised manuscript**]

Page 9 (5 Temperature measurement example (2 October 2014))

Instead of

"Figure 12 shows a temperature profile retrieved using Eq. (11). For this profile in the 3–12km altitude region we have: $\Delta\overline{T}$ < 0.7 K, $(\overline{\Delta T / T})$ < 0.006, and $|T_{\mathrm{CPAC}} - T|$ < 6.5 K. Figure 13 shows temperature profiles retrieved using Eqs. (13) and (18). The temperature profiles retrieved using Eqs. (15) and (20) are presented in Fig. 14. As seen from Figs. 13 and 14, $\Delta\overline{T}$ < 1.6 K, $(\overline{\Delta T / T})$ < 0.014, and $|T_{\mathrm{CPAC}} - T|$ < 3.0 K when applying Eq. (13); and $\Delta\overline{T}$ < 0.8 K, $(\overline{\Delta T / T})$ < 0.008, and $|T_{\mathrm{CPAC}} - T|$ < 1.8 K for Eq. (20) in the 3–12km altitude region."

we wrote

"Figure 12 shows a temperature profile retrieved using Eq. (11). For this profile in the 3–12km altitude region we have: $\Delta\overline{\overline{T}}$ < 1 K, $(\overline{\overline{\Delta T / T}})$ < 0.005, and $|T_{\mathrm{CPAC}} - T|$ < 6.5 K. Figure 13 shows temperature profiles retrieved using Eqs. (13) and (18). The temperature profiles retrieved using Eqs. (15) and (20) are presented in Fig. 14. As seen, e.g., in Fig. 14, $\Delta\overline{\overline{T}}$ < 1.8 K, $(\overline{\overline{\Delta T / T}})$ < 0.009, and $|T_{\mathrm{CPAC}} - T|$ < 2.9 K when applying Eq. (15); and $\Delta\overline{\overline{T}}$ < 1.3 K, $(\overline{\overline{\Delta T / T}})$ < 0.007, and $|T_{\mathrm{CPAC}} - T|$ < 1.8 K for Eq. (20) in the 3–12km altitude region. The comparative analysis of the parameters is presented in Fig. 15."

[**Page 9, lines 24–28, revised manuscript**]

Page 10 (6 Summary and outlook)

Instead of

"The comparative analysis of three parameters $\Delta\overline{T}$, $(\overline{\Delta T / T})$, and $|T_{\mathrm{CPAC}} - T|$ showed:"

we wrote

"For the case of the IMCES PRR lidar system, the comparative analysis of three parameters $\Delta\overline{\overline{T}}$, $(\overline{\overline{\Delta T / T}})$, and $|T_{\mathrm{CPAC}} - T|$ showed the following:"

[**Page 10, lines 18 and 19, revised manuscript**]

Pages 10 and 11 (6 Summary and outlook)

Instead of

"As the best function for temperature retrievals can depend on a lidar system (e.g., based on DGs or IFs for PRR lines extracting), it is reasonable to check all the mentioned nonlinear functions against lidar data obtained with different lidar systems to determine the best function in each specific case. As the collisional broadening of PRR lines is the largest in the atmospheric boundary layer, the nonlinear calibrations functions should be applied instead of the linear one for temperature retrievals, especially if using a coaxial lidar. Furthermore, the stability of the calibration functions coefficients during long-time lidar measurements is one of the crucial aspects in determination of the best function. Therefore, it would be a good thing to study the coefficients stability during a day, week, month, etc., as well as it was done in (Lee III, 2013) for the linear calibration function coefficients."

we wrote

"As it was mentioned above (Sect. 4.2), the CPAC points can hardly be used as the reference data to reliably calibrate PRR lidars and retrieve accurate temperature profiles. Nevertheless, the results suggest that the best-suited calibration function for temperature retrievals can depend on the lidar system (e.g., based on DGs or IFs for PRR lines extracting), which can take into account the collisional broadening of PRR lines in varying degrees. Indeed, the calibration errors depend on the spectral characteristics of the lidar receiver such as the central wavelength, shape and width of the transmission functions, as well as whether just the anti-Stokes (IFs) or both branches of the PRR spectrum (DGs) are used to extract the PRR signals from backscattered light. Therefore, it is reasonable to check all the mentioned nonlinear functions against lidar data obtained with different lidar systems to determine the best function in each specific case. Furthermore, the stability of the calibration functions coefficients during long-time lidar measurements is one of the crucial aspects in determination of the best function. Hence, it would be a good thing to study the coefficients stability during a night (Jia and Yi, 2014; Li et al., 2015), week, month, etc., as it was done in (Lee III, 2013) for the linear calibration function coefficients."

[**Page 10, lines 26–31 and Page 11, lines 1–5, revised manuscript**]

As Appendix A was substantially rewritten, see it please in the revised manuscript.

Page 14 (Appendix A0: Linear calibration function)

Instead of

"For definiteness, we use Eqs. (A12) and (A13) to derive the absolute and relative uncertainties in an analytical form."

we wrote

"As we applied the first way of the second-order averaging of the IMCES lidar raw data (see Appendix A and Sect. 4.1), we use Eqs. (A9) and (A10) to derive the absolute and relative uncertainties in an analytical form. In case of the first-order averaging of lidar raw data, one can use Eqs. (A5) and (A6), respectively."

[**Page 15, lines 8–11, revised manuscript**]

Page 25 (Figure 1 caption)

The following explaining sentences were added to the manuscript:

"The red and blue envelopes correspond to the temperature of 280 and 220 K, respectively. The laser beam wavelength is 354.67 nm."

Page 32 (Figure 10 caption)

"**Figure 10.** (1 April 2015) Comparative analysis of the absolute temperature uncertainties yielded by using Eqs. (A27), (A33), (A40), and (A47), and of the difference in modulus between temperature values retrieved from the CPACs and IMCES lidar data."

Page 35 (Figure 15 caption)

"**Figure 15.** (2 October 2014) Comparative analysis of the absolute temperature uncertainties yielded by using Eqs. (A27), (A33), (A40), and (A47), and of the difference in modulus between temperature values retrieved from the CPACs and IMCES lidar data."

Sincerely,

Authors

Tropospheric temperature retrievals using nonlinear calibration functions in the frame of the pure rotational Raman lidar technique

Vladimir V. Zuev[1,2,3], Vladislav V. Gerasimov[1,2], Vladimir L. Pravdin[1], Aleksei V. Pavlinskiy[1], and Daria P. Nakhtigalova[1]

[1]Institute of Monitoring of Climatic and Ecological Systems SB RAS, Tomsk, 634055, Russia
[2]Tomsk State University, Tomsk, 634050, Russia
[3]Tomsk Polytechnic University, Tomsk, 634050, Russia

Correspondence to: Vladislav V. Gerasimov (gvvsnake@mail.ru)

Abstract. Among lidar techniques, the pure rotational Raman (PRR) technique is the best-suited for tropospheric and lower stratospheric temperature measurements. Calibration functions are required for the PRR technique to retrieve temperature profiles from lidar remote sensing data. Both temperature retrieval accuracy and number of calibration coefficients depend on the selected function. The commonly used calibration function (linear in reciprocal temperature 1/*T* with two calibration coefficients) ignores all types of broadening of individual PRR lines of atmospheric N_2 and O_2 molecules. However, the collisional (pressure) broadening dominates over other types of broadening of PRR lines in the troposphere and can differently affect the accuracy of tropospheric temperature measurements depending on the PRR lidar system. We recently derived the calibration function in the general analytical form that takes into account the collisional broadening of all N_2 and O_2 PRR lines (Gerasimov and Zuev, 2016). This general calibration function represents an infinite series and, therefore, cannot be directly used in the temperature retrieval algorithm. For this reason, its four simplest special cases (calibration functions nonlinear in 1/*T* with three calibration coefficients), two of which have not been suggested before, were considered and analyzed. All the special cases take the collisional PRR lines broadening into account in varying degrees and the best function among them was determined via simulation. In this paper, we use the special cases to retrieve tropospheric temperature from real PRR lidar data. The calibration function best-suited for tropospheric temperature retrievals is determined from the comparative analysis of temperature uncertainties yielded by using these functions. The absolute and relative statistical uncertainties of temperature retrieval are given in an analytical form assuming Poisson statistics of photon counting. The vertical tropospheric temperature profiles, retrieved from nighttime lidar measurements in Tomsk (56.48° N, 85.05° E, Western Siberia, Russia) on 2 October 2014 and 1 April 2015, are presented as an example of the calibration functions application. The measurements were performed using a PRR lidar designed in the Institute of Monitoring of Climatic and Ecological Systems of the Siberian Branch of the Russian Academy of Sciences for tropospheric temperature measurements.

1 Introduction

The pure rotational Raman (PRR) technique is known to be the best-suited for lower atmosphere temperature measurements (Wulfmeyer et al., 2015). The retrieval algorithm of vertical temperature profiles of the troposphere and lower stratosphere from PRR lidar raw signals consists of four main steps:

1. PRR lidar raw data averaging to improve the signal-to-noise ratio and decrease the statistical uncertainties;
2. Lidar calibration, i.e. determination of the lidar calibration function coefficients by applying, e.g., the least square method to the reference radiosonde (or model) data and previously averaged lidar data;
3. Temperature profile retrieval by using the temperature retrieval function derived from the selected calibration function;
4. Estimation of the absolute and relative uncertainties of the temperature retrieval, and calculation of the difference between the reference temperature (radiosonde, model) and temperature retrieved from lidar data.

The PRR lidar technique suggested by Cooney (1972) is based on the temperature dependence of individual lines intensity of atmospheric N_2 and O_2 PRR spectra. The intensity $I(T, \lambda)$ of a single PRR line of the wavelength λ backscattered by excited N_2 or O_2 molecules can be expressed as (Penney et al., 1974)

$$I(\lambda, T) = PL\beta_\pi(\lambda, T), \tag{1}$$

where P is the incident laser beam power; L is the length of the scattering volume; $\beta_\pi(\lambda, T)$ is the backscatter cross section (atmospheric backscatter coefficient). The backscattered signals of the Stokes and/or anti-Stokes branches of the spectra can be used for temperature determination. The intensities of individual PRR lines, corresponding to low and high rotational quantum numbers J of the initial states of the PRR transitions, are of opposite temperature dependence (Behrendt, 2005). Namely, the intensity of each N_2 PRR line with $J_{\text{low}} \leq 8$ ($J_{\text{low}} \leq 9$ for O_2 PRR lines) decreases with increasing temperature, and conversely, the intensity of N_2 PRR lines with $J_{\text{high}} \geq 9$ ($J_{\text{high}} \geq 11$ for O_2 PRR lines) increases with increasing temperature, in both branches of the spectra (Fig. 1). Note that only odd lines beginning with odd J exist in O_2 PRR spectrum (Wandinger, 2005). A ratio of backscattered signal intensities from two PRR-spectrum bands with opposite temperature dependence is required for air temperature T determination. However, the PRR lidar theory (Cooney, 1972) gives the exact temperature dependence only for intensity ratios of two individual PRR lines corresponding to certain J_{low} and J_{high}

$$Q^{\text{indiv.}}(T) = \frac{I(J_{\text{low}}, T)}{I(J_{\text{high}}, T)} = \frac{\beta_\pi(J_{\text{low}}, T)}{\beta_\pi(J_{\text{high}}, T)} = \exp\left(\alpha + \frac{\beta}{T}\right), \tag{2}$$

where the constants α and β are completely defined from the theory.

In practice, diffraction gratings (DGs) or interference filters (IFs) extract several adjacent PRR lines in the lidar temperature channels from backscattered light. IFs extract PRR lines from the anti-Stokes branches of N_2 and O_2 PRR spectra (Behrendt and Reichardt, 2000; Behrendt et al., 2002; Alpers et al., 2004; Di Girolamo et al., 2004; Radlach et al., 2008; Achtert et al., 2013; Newsom et al., 2013; Behrendt et al., 2015; Li et al., 2015). DGs extract PRR lines from both the Stokes and anti-Stokes branches of the spectra (Ansmann et al., 1999; Kim et al., 2001; Chen et al., 2011; Jia and Yi, 2014). Thus, one should consider the following expression (Arshinov et al., 1983)

$$Q^{\Sigma}(T) = \frac{I^{\Sigma}_{\text{low}}(T)}{I^{\Sigma}_{\text{high}}(T)} = \frac{\left[\sum_{J_{\text{N}_2}} \beta_{\pi}(J_{\text{N}_2}, T) + \sum_{J_{\text{O}_2}} \beta_{\pi}(J_{\text{O}_2}, T)\right]_{\text{low}}}{\left[\sum_{J_{\text{N}_2}} \beta_{\pi}(J_{\text{N}_2}, T) + \sum_{J_{\text{O}_2}} \beta_{\pi}(J_{\text{O}_2}, T)\right]_{\text{high}}}, \tag{3}$$

where $\beta_{\pi}(J_{\text{N}_2}, T)$ and $\beta_{\pi}(J_{\text{O}_2}, T)$ are the backscatter coefficients corresponding to N_2 and O_2 individual PRR lines, respectively; $I^{\Sigma}_{\text{low}}(T)$ and $I^{\Sigma}_{\text{high}}(T)$ are the overall intensities of the PRR lines which enter the corresponding lidar temperature channels; indexes "low" and "high" show that summations in the numerator and denominator refer to the corresponding PRR-spectrum bands with J_{low} and J_{high}. The ratio $Q^{\Sigma}(T)$ in Eq. (3) has a complicated temperature dependence and cannot be expressed as a simple function of T. For this reason, an approximation (calibration) function $f_c^{\Sigma}(T)$ for the ratio $Q^{\Sigma}(T)$ is required to retrieve temperature profiles from lidar remote sensing data (Behrendt, 2005). The temperature retrieval accuracy and number of calibration coefficients depend on the selected calibration function.

Assuming that each PRR line profile represents the Dirac function, the general calibration function can be written in a natural logarithm form as follows (Gerasimov and Zuev, 2016)

$$\ln Q^{\Sigma}(T) \approx \ln f_c^{\Sigma}(T) = A + \frac{B}{T} + \frac{C}{T^2} + \frac{D}{T^3} + \cdots \quad \Leftrightarrow \quad y = A + Bx + Cx^2 + Dx^3 + \cdots, \tag{4}$$

where A, B, C, D, etc. are the calibration (fit) coefficients determined by applying the least square method to lidar remote sensing (or simulation) data and reference radiosonde (or model) data; the symbol $\Leftrightarrow$ denotes the equivalence of expressions; $x = 1/T$ is the reciprocal temperature. The n-order in x polynomial is assumed to retrieve temperature profiles with any desired accuracy depending on n (Di Girolamo et al., 2004). The linear in x special case of Eq. (4) with two calibration coefficients A and B (Arshinov et al., 1983) and the second-order in x polynomial with three calibration coefficients A, B and C (Behrendt and Reichardt, 2000) are usually used by lidar researchers for temperature retrievals in the troposphere and lower stratosphere. However, N_2 and O_2 PRR lines are broadened by the Doppler and molecular collision effects. Hence, their backscatter profiles are described by a Voigt function, which is a convolution of certain Gaussian and Lorentzian functions (Nedeljkovic et al., 1993). As the molecular collision effect dominates over the Doppler effect in the troposphere (Ivanova et al., 1993), one can consider the Lorentzian function for a PRR line shape description instead of the Voigt one (Ginzburg, 1972). Therefore, all collisionally broadened PRR lines contribute to the signals detected in both lidar temperature channels due to the long Lorentzian tails of the line profiles (Measures, 1984), and the general calibration function takes on the form (Gerasimov and Zuev, 2016)

$$\ln Q^{\text{all}}(T) = \cdots + \frac{A_{-2}}{T} + \frac{A_{-1}}{\sqrt{T}} + A_0 + A_1\sqrt{T} + A_2 T + \cdots = \sum_{n=-\infty}^{\infty} A_n T^{\frac{n}{2}}, \tag{5}$$

where A_n are the calibration coefficients and Eq. (4) represents a special case of Eq. (5). All the calibration functions mentioned above are valid only when the parasitic elastic signal backscattered by atmospheric aerosols and molecules is sufficiently suppressed in the lidar temperature channels. The state-of-the-art narrow-band IFs and DGs provide the suppression of the parasitic signal intensity in the channels up to 8–10 orders of magnitude (Achtert et al., 2013; Hammann and Behrendt, 2015; Hammann et al., 2015).

In order to take into account the atmospheric extinction of backscattered signals and their losses in the lidar transmitting and receiving optics, one should consider the lidar equation (Measures, 1984)

$$N(\lambda, z, T) = \eta N_0 G(\lambda, z) \frac{c\tau_0}{2} \xi(\lambda) \frac{A}{z^2} \beta_\pi(\lambda, z, T) \Theta^2(\lambda, z), \tag{6}$$

where $N(\lambda,z,T)$ is the number of backscattered photons (photocounts) detected by a photomultiplier tube (PMT) in a lidar temperature channel; N_0 is the number of emitted photons; η is the PMT quantum efficiency; $G(\lambda, z)$ is the laser-beam receiver-field-of-view overlap; τ_0 is the laser pulse duration; c is the speed of light; $\xi(\lambda)$ is the transmittance of the lidar receiving optical system; A is the receiver telescope area; z is the scattering region altitude; and $\Theta(\lambda, z)$ is the transmission coefficient through the atmosphere between the scattering region and the lidar. Taking Eqs. (5) and (6) into account, the ratio of the background-subtracted photocounts N_L and N_H from two spectrally close bands involving several N_2 and O_2 PRR lines with J_low and J_high becomes (Newsom et al., 2012; Newsom et al., 2013)

$$Q(T, z) = \frac{N_\text{L}(T, z)}{N_\text{H}(T, z)} = \frac{G_\text{L}(z)}{G_\text{H}(z)} \exp\left(\sum_{n=-\infty}^{\infty} B_n T^{\frac{n}{2}}\right) = O(z) \exp\left(\sum_{n=-\infty}^{\infty} B_n T^{\frac{n}{2}}\right), \tag{7}$$

where B_n are the calibration coefficients; $O(z) = G_\text{L}(z)/G_\text{H}(z)$ is the laser-beam receiver-field-of-view overlap function. At the complete overlap altitudes (usually above the atmospheric boundary layer), where $O(z) = 1$, Eq. (7) goes over into the calibration function like Eq. (5)

$$\ln Q(T) = \sum_{n=-\infty}^{\infty} B_n T^{\frac{n}{2}}. \tag{8}$$

Note that the same result can be obtained on the assumption that the collisionally broadened elastic backscattered signal leaks into the nearest (to the laser line) lidar temperature channel (Gerasimov et al., 2015).

In our recent Optic Express paper, we considered the physics of our approach, derived mathematically the general calibration function that takes into account the collisional broadening of all N_2 and O_2 PRR lines, analyzed four nonlinear three-coefficient special cases of Eq. (8) via simulation to be used in the temperature retrieval algorithm, and determined the best function among them. In this paper, we apply these calibration functions to real lidar remote sensing data. The calibration function best-suited for tropospheric temperature retrievals (for our PRR lidar system) is determined from the comparative analysis of temperature uncertainties yielded by using these functions.

2 Special cases of the general calibration function

The general calibration function expressed by Eq. (8) represents an infinite series, and hence, the temperature retrieval function $T = T(Q)$ cannot be obtained in an analytical form from this series. Therefore, one can use, e.g., some special cases of the integer power approximation of Eq. (8), i.e.

$$\ln Q(T) \approx \cdots + \frac{C_{-2}}{T^2} + \frac{C_{-1}}{T} + C_0 + C_1 T + C_2 T^2 + \cdots = \sum_{n=-\infty}^{\infty} C_n T^n, \tag{9}$$

where C_n are the calibration coefficients which can differ from B_n in Eq. (8). Here we consider the linear and four simplest nonlinear (in reciprocal temperature $1/T$) calibration functions and their corresponding temperature retrieval functions. Since Eq. (9) is a special case of Eq. (8), any special case of Eq. (9) automatically represents a special case of Eq. (8). The absolute and relative uncertainties of indirect temperature measurements are obtained in an analytical form in Appendices A, A0–A4.

The frequently-used calibration function linear in $x = 1/T$ (Arshinov et al., 1983) is a special case of Eq. (9)

$$\ln Q = A_0 + \frac{B_0}{T} \Leftrightarrow y = A_0 + B_0 x, \tag{10}$$

and its corresponding temperature retrieval function is

$$T = \frac{B_0}{\ln Q - A_0}, \tag{11}$$

where A_0 and B_0 are the commonly designated calibration constants.

The most used nonlinear calibration function (Behrendt and Reichardt, 2000), containing the term quadratic in $x = 1/T$, also represents a special case of Eq. (9), i.e.

$$\ln Q = A_1 + \frac{B_1}{T} + \frac{C_1}{T^2} \Leftrightarrow y = A_1 + B_1 x + C_1 x^2, \tag{12}$$

where A_1, B_1, and C_1 are the calibration constants. The corresponding temperature retrieval function is simply derived from Eq. (12)

$$T = \frac{2C_1}{-B_1 + \sqrt{B_1^2 + 4C_1\left(\ln Q - A_1\right)}}. \tag{13}$$

Another three-coefficient special case of Eq. (9) can be written as follows (Gerasimov and Zuev, 2016)

$$\ln Q = A_2 + \frac{B_2}{T} + C_2 T \;\Leftrightarrow\; y = A_2 + B_2 x + \frac{C_2}{x}, \tag{14}$$

where A_2, B_2, and C_2 are the calibration constants. Solving Eq. (14), we have for the temperature retrieval function

$$T = \frac{2B_2}{(\ln Q - A_2) + \sqrt{(\ln Q - A_2)^2 - 4B_2 C_2}}. \tag{15}$$

As it follows from the PRR lidar theory (Cooney, 1972), $y = \ln Q$ is a linear function of reciprocal temperature $x = 1/T$ (Arshinov et al., 1983). Conversely, the reciprocal temperature represents a linear function of $\ln Q$, i.e. $x = a + by$. In order to take nonlinear effects into account, we consider the function

$$x = a + by + cy^2 \;\Leftrightarrow\; \frac{1}{T} = a + b\ln Q + c(\ln Q)^2, \tag{16}$$

where a, b, and c are some constants. Thus, a temperature profile can simply be retrieved via

$$T = \left[c(\ln Q)^2 + b\ln Q + a\right]^{-1} \tag{17}$$

or

$$T = \frac{C_3}{(\ln Q)^2 + B_3 \ln Q + A_3}, \tag{18}$$

where $A_3 = a/c$, $B_3 = b/c$, and $C_3 = 1/c$. Equation (18) was first applied to real lidar data by Lee III (2013). Note that Eq. (16) represents a special case of Eq. (8), as we showed in our 2016 paper.

There exists another way to represent collisional PRR lines broadening (and therefore, nonlinear effects). Adding a term hyperbolic in $y = \ln Q$ to the linear calibration function of the form $x = a + by$ gives

$$x = A_4 + B_4 y + \frac{C_4}{y} \;\Leftrightarrow\; \frac{1}{T} = A_4 + B_4 \ln Q + \frac{C_4}{\ln Q}, \tag{19}$$

where A_4, B_4, and C_4 are the calibration constants. Solving Eq. (19) yields

$$T = \frac{1}{A_4 + B_4 \ln Q + (C_4/\ln Q)} = \frac{\ln Q}{B_4 (\ln Q)^2 + A_4 \ln Q + C_4}. \tag{20}$$

All the nonlinear calibration (or temperature retrieval) functions considered here take into account in varying degrees the collisional PRR lines broadening.

3 The IMCES lidar setup

The IMCES PRR lidar was developed in the Institute of Monitoring of Climatic and Ecological Systems of the Siberian Branch of the Russian Academy of Sciences (IMCES SB RAS) for nighttime tropospheric temperature measurements. A frequency-tripled Nd:YAG laser operating at a wavelength of 354.67 nm with 105mJ pulse energy at a pulse repetition rate of 20 Hz is used as the lidar transmitter. The backscattered signals (photons) are collected by a prime-focus receiving telescope with a mirror diameter of 0.5 m. The IMCES lidar optical layout is shown in Fig. 2. The selection of spectrum bands containing PRR lines with J_{low} and J_{high} from both the Stokes and anti-Stokes branches of N_2 and O_2 PRR-spectra (Fig. 1) is performed via a double-grating monochromator (DGM). The DGM design and arrangement of optical fibers connecting both DGM blocks are the same as suggested by Ansmann et al. (1999). The main technical parameters of the IMCES lidar transmitting, receiving, and data acquisition systems are summarized in Table 1. The spectral selection parameters of the DGM channels are listed in Table 2.

4 Temperature measurement example (1 April 2015)

In this section we consider an example of nighttime tropospheric temperature measurements performed with the IMCES lidar on 1 April 2015 in Tomsk (56.48° N, 85.05° E, Western Siberia, Russia). The lidar data were taken from 03:45 to 05:15 LT (or 31 March, 21:45–23:15 UTC), i.e. within 90 min integration time (108,000 laser shots). In order to determine the best calibration function that yields the minimum temperature retrieval uncertainties, we compare and analyze five vertical tropospheric temperature profiles retrieved from the lidar data using Eqs. (11), (13), (15), (18), and (20).

4.1 Raw lidar data averaging

In order to improve the signal-to-noise ratio, raw lidar data (background-subtracted photocounts N_{L} and N_{H} detected by PMTs in the DGM channels) should be averaged. We tested more than dozens of different data-averaging methods including the equal-sized and variable sliding-window averaging ones presented in various papers (Behrendt and Reichardt, 2000; Behrendt et al., 2002; Alpers et al., 2004; Di Girolamo et al., 2004; Radlach et al., 2008; Radlach, 2009; Jia and Yi, 2014). The optimal data-averaging method for our lidar system is the following. The IMCES lidar raw data with vertical resolution of Δz = 24 m are averaged with a variable sliding average window (Appendix A). Having an initial size of $n = 2k + 1 = 3$ (k = 1), the sliding window is increased by one point on either side of the central point for every ten data points. Otherwise, starting with an initial length of $\Delta\bar{z} = n\Delta z = 72$ m in the lidar to 240m altitude range, the sliding window is increased above and below by 24 m for every 240m increase in altitude (see Fig. 3a). For example, the sliding window size and length (or averaged data resolution) are of n = 27 (k = 13) and $\Delta\bar{z} = 648$ m at an altitude of 3 km, and n = 85 (k = 42) and $\Delta\bar{z} = 2040$ m at an altitude of 10 km, respectively. Note that similar lidar-data-averaging procedure was used, e.g., in (Lee III, 2013). Due to low power of the IMCES lidar laser, the ratio of single-averaged signals (i.e. $Q = \bar{N}_{\mathrm{L}} / \bar{N}_{\mathrm{H}}$) was additionally slightly averaged with a small equal-sized sliding window (l = 5, and m = 11 in Eq. A7) to reduce signal statistical fluctuations (Fig. 3b, see also the Supplement). For example, the double-averaged data resolution becomes $\Delta\overline{\overline{z}} = [2(k+l)+1]\Delta z = 2280$ m (k = 42, l = 5) at an altitude of 10 km, but both absolute and relative statistical uncertainties additionally decrease by $\sqrt{m} = \sqrt{11}$ times (Appendix A). For any other lidar system, the optimal data-averaging method can differ from the method we used.

4.2 Reference temperature points for the lidar calibration

One of the problems we face during temperature measurements is the following. Unfortunately, we do not have our own radiosondes, and therefore, we have no possibility to launch a radiosonde simultaneously with lidar remote sensing at the lidar site. The two nearest to Tomsk meteorological stations launching radiosondes twice a day are situated in Novosibirsk (55.02° N, 82.92° E) and Kolpashevo (58.32° N, 82.92° E). Both these towns are at a distance of more than 250 km from Tomsk. Hence, we cannot directly use vertical temperature profiles from these radiosondes as reference data points, which are known to be required for PRR lidars calibration. However, we solved this problem as follows. We retrieved several points over Tomsk with the temperature accuracy of 0.5 K and the vertical accuracy of 20 m using the 925, 850, 700, 500, 400, 300, 200, and 100 hPa constant pressure altitude charts (CPACs), which can be found on http://gpu.math.tsu.ru/maps/. Several CPACs are presented in the Supplement as an example. Two temperature profiles from radiosondes, launched on 1 April 2015 at 06:00 LT (00:00 UTC) in Novosibirsk and Kolpashevo, together with temperature points over Tomsk retrieved from the CPACs are shown in Fig. 4. The radiosondes data are presented only for comparison and can be found on the webpage http://weather.uwyo.edu/upperair/sounding.html?region=np of the University of Wyoming (Novosibirsk and Kolpashevo station numbers are 29634 and 29231, respectively). It is clear that the CPAC points are not suitable for using them as the reference points to calibrate lidars and retrieve temperature profiles with high accuracy (for this purpose the local radiosonde data are required). Nevertheless, the accuracy of these points (0.5 K, 20 m) is sufficient to make the comparative analysis of temperature uncertainties, yielded by using different calibration functions, and determine the best-suited function (among them) for our lidar system.

4.3 Temperature profiles retrieved with different calibration functions

Here we compare nighttime temperature profiles retrieved using five calibration functions considered in Sect. 2 from the altitude where the laser-beam receiver-field-of-view overlap is complete (~3 km) to 13 km (i.e. slightly above the local tropopause). Figure 5 presents a tropospheric temperature profile retrieved using the temperature retrieval function (Eq. 11) derived from the standard linear calibration function (Eq. 10). The absolute statistical uncertainty $\Delta\overline{\overline{T}}$ of temperature retrieval is calculated by Eq. (A21), whereas the relative uncertainty $(\overline{\overline{\Delta T / T}})$ is calculated by Eq. (A22). The difference in modulus $|T_{\mathrm{CPAC}} - T|$ between temperature values retrieved from the CPACs and IMCES lidar data is also presented in Fig. 5. The nearest radiosondes data are given for comparison. Figures 6–9 show temperature profiles retrieved using the temperature retrieval functions expressed by Eqs. (13), (15), (18), and (20), respectively. These functions are derived from the corresponding nonlinear calibration functions, i.e. Eqs. (12), (14), (16), and (19).

Comparing all five profiles among themselves, one can see that, despite the lowest values of both the statistical uncertainties in the 3–12km altitude region ($\Delta\overline{\overline{T}}$ < 0.7 K, $(\overline{\overline{\Delta T / T}})$ < 0.004) yielded by using Eq. (11), the difference $|T_{\mathrm{CPAC}} - T|$ can reach ~5.5 K (Fig. 5). For the nonlinear functions in the same altitude region, the maximum difference $|T_{\mathrm{CPAC}} - T|$ is less than 2.2 and ~0.9 K when using Eq. (13) and Eq. (20), respectively, as seen in Figs. 6, 9 and 10 (see also the Supplement). Similarly, for both the uncertainties we have: $\Delta\overline{\overline{T}}$ < 2.3 K, $(\overline{\overline{\Delta T / T}})$ < 0.011 when applying Eq. (13), and $\Delta\overline{\overline{T}}$ < 1 K, $(\overline{\overline{\Delta T / T}})$ < 0.005 for Eq. (20). Note that the peaks of curves $\Delta\overline{\overline{T}}$ and $(\overline{\overline{\Delta T / T}})$ near 11km altitude in Figs. 6 and 7 are caused by the problem with square roots in Eqs. (13) and (15) described in Appendices A1 and A2. There is no such problem in case of Eqs. (18) and (20) without square roots. The tropopause is also located near 11km altitude. Taking into account all three parameters $\Delta\overline{\overline{T}}$, $(\overline{\overline{\Delta T / T}})$, and $|T_{\mathrm{CPAC}} - T|$, we can conclude that Eqs. (13), (15), (18), and (20) retrieve the tropospheric temperature much better compared to Eq. (11). Moreover, the functions expressed by Eqs. (18) and (20) yield the smallest uncertainties and $|T_{\mathrm{CPAC}} - T|$ values among considered nonlinear functions, and therefore, they are the best-suited for tropospheric temperature retrievals with the IMCES PRR lidar.

5 Temperature measurement example (2 October 2014)

Let us consider another example of nighttime tropospheric temperature measurements performed with the IMCES PRR lidar on 2 October 2014 in Tomsk. The lidar data were taken from 20:21 to 21:21 LT (13:21–14:21 UTC), i.e. within 60 min integration time (72,000 laser shots). The raw and averaged IMCES lidar signals together with raw and averaged signal ratios are presented in Fig. 11. Here also we compare five temperature profiles retrieved using Eqs. (11), (13), (15), (18), and (20). The temperature retrieval algorithm is the same as was applied to the IMCES lidar data dated 1 April 2015. For the lidar calibration, we retrieved temperature points over Tomsk using the corresponding CPACs. Two temperature profiles from radiosondes, launched on 2 October 2014 at 19:00 LT (12:00 UTC) in Novosibirsk and Kolpashevo, are also given for comparison.

Figure 12 shows a temperature profile retrieved using Eq. (11). For this profile in the 3–12km altitude region we have: $\Delta\overline{\overline{T}}$ < 1 K, $(\overline{\overline{\Delta T / T}})$ < 0.005, and $|T_{\mathrm{CPAC}} - T|$ < 6.5 K. Figure 13 shows temperature profiles retrieved using Eqs. (13) and (18). The temperature profiles retrieved using Eqs. (15) and (20) are presented in Fig. 14. As seen, e.g., in Fig. 14, $\Delta\overline{\overline{T}}$ < 1.8 K, $(\overline{\overline{\Delta T / T}})$ < 0.009, and $|T_{\mathrm{CPAC}} - T|$ < 2.9 K when applying Eq. (15); and $\Delta\overline{\overline{T}}$ < 1.3 K, $(\overline{\overline{\Delta T / T}})$ < 0.007, and $|T_{\mathrm{CPAC}} - T|$ < 1.8 K for Eq. (20) in the 3–12km altitude region. The comparative analysis of the parameters is presented in Fig. 15. The tropopause is located near 12.3km altitude. Comparing pairwise all the retrieved profiles for both measurement examples, one can see that $\overline{\overline{\Delta T}}$, $(\overline{\overline{\Delta T / T}})$, and $\left|T_{\mathrm{CPAC}} - T\right|$ values in case of the second example (2 October 2014) are higher than that for the first one (1 April 2015, Sect. 4.3). This is due to that the smaller number of laser shots (and, therefore, photocounts detected in both DGM channels) leads to the higher absolute and relative statistical uncertainties, as seen from Eqs. (A9) and (A10) in Appendix A. The two best-suited functions for temperature retrievals are seen in Figs. 13 and 14 to be the same as in the previous example (1 April 2015). The large difference between the CPAC and lidar temperature values in 2 to 3 km altitude region (Figs. 5 and 12; see also Lee III, 2013) is, perhaps, due to the incomplete laser-beam receiver-field-of-view overlap in the region. We also cannot exclude that any of the nonlinear calibration functions is able to somehow correct for this incomplete overlap in the atmospheric boundary layer.

The calibration coefficients of all the calibration functions used in both the temperature measurement examples can be found in the Supplement.

6 Summary and outlook

We have considered and used the linear and four nonlinear (three-coefficient) in $x = 1/T$ calibration functions in the tropospheric temperature retrieval algorithm. The corresponding temperature retrieval functions were applied to the nighttime temperature measurement data obtained with the IMCES PRR lidar on 2 October 2014 and 1 April 2015. We have also derived and used the absolute and relative statistical uncertainties of indirect temperature measurements in an analytical form (Appendices A, A0–A4).

For the case of the IMCES PRR lidar system, the comparative analysis of three parameters $\overline{\overline{\Delta T}}$, $(\overline{\overline{\Delta T / T}})$, and $\left|T_{\mathrm{CPAC}} - T\right|$ showed the following:

- the nonlinear functions expressed by Eqs. (13), (15), (18), and (20) retrieve the tropospheric temperature much better compared to the linear function (Eq. 11);
- equations (18) and (20) give the almost equally best-suited functions for the tropospheric temperature retrievals (although, Eq. 20 is slightly better than Eq. 18);
- the function given by Eq. (18) is the best from both practical (real lidar data) and theoretical (simulation) points of view (Gerasimov and Zuev, 2016).

As it was mentioned above (Sect. 4.2), the CPAC points can hardly be used as the reference data to reliably calibrate PRR lidars and retrieve accurate temperature profiles. Nevertheless, the results suggest that the best-suited calibration function for temperature retrievals can depend on the lidar system (e.g., based on DGs or IFs for PRR lines extracting), which can take into account the collisional broadening of PRR lines in varying degrees. Indeed, the calibration errors depend on the spectral characteristics of the lidar receiver such as the central wavelength, shape and width of the transmission functions, as well as whether just the anti-Stokes (IFs) or both branches of the PRR spectrum (DGs) are used to extract the PRR signals from backscattered light. Therefore, it is reasonable to check all the mentioned nonlinear functions against lidar data obtained with different lidar systems to determine the best function in each specific case. Furthermore, the stability of the calibration functions coefficients during long-time lidar measurements is one of the crucial aspects in determination of the best function. Hence, it would be a good thing to study the coefficients stability during a night (Jia and Yi, 2014; Li et al., 2015), week, month, etc., as it was done in (Lee III, 2013) for the linear calibration function coefficients.

Appendix A: Absolute and relative uncertainties of temperature retrieval

Each value T of a temperature profile retrieved from raw lidar data is known to be within the confidence interval [$T - \Delta T$; $T + \Delta T$], where $\Delta T > 0$. Assuming Poisson statistics of photon counting, the 1–σ absolute statistical uncertainty ΔT of indirect temperature measurements is defined in the general form as (Behrendt, 2005; Radlach, 2009)

$$\Delta T = \sqrt{\left(\frac{dT}{dQ}\Delta Q\right)^2} = \left|\frac{dT}{dQ}\right| Q \sqrt{\frac{1}{N_\mathrm{H}} + \frac{1}{N_\mathrm{L}}}, \tag{A1}$$

where the temperature retrieval function $T = T(Q)$ is derived from any required calibration function (see Sect. 2); $Q = N_\mathrm{L}/N_\mathrm{H}$ is the ratio of the background-subtracted photocounts N_L and N_H registered in the lidar temperature channels with J_low and J_high, respectively. Consequently, the relative statistical uncertainty ($\Delta T/T$) of indirect temperature measurements is simply derived from Eq. (A1)

$$\left(\frac{\Delta T}{T}\right) = \left|\frac{dT}{dQ}\right| \frac{Q}{T} \sqrt{\frac{1}{N_\mathrm{H}} + \frac{1}{N_\mathrm{L}}}. \tag{A2}$$

However, Eqs. (A1) and (A2) are valid only for unaveraged (raw) lidar data N_L and N_H. In practice, raw data are previously averaged to improve the signal-to-noise ratio. One of the most simple and used data-averaging methods is the equal-sized (or variable) sliding-window averaging (Behrendt and Reichardt, 2000; Behrendt et al., 2002; Alpers et al., 2004; Di Girolamo et al., 2004; Radlach et al., 2008; Radlach, 2009; Lee III, 2013). The averaged data $\overline{N}(z)$ and their variance $\overline{\mathrm{Var}}(z)$ are related to the corresponding unaveraged data $N(z)$ and variance Var(z) as follows (El'nikov et al., 2000)

$$\begin{aligned}\overline{N}_j(z) &= \frac{1}{2k+1}\sum_{i=-k}^{k} N_{j+i} = \frac{1}{2k+1}\sum_{i=-k}^{k} N(z+i\Delta z) \\ &= \frac{1}{n}\left[N(z-k\Delta z) + \cdots + N(z) + \cdots + N(z+k\Delta z)\right],\end{aligned} \tag{A3}$$

$$\overline{\mathrm{Var}}(z) = \mathrm{Var}(z)/n, \tag{A4}$$

where Δz is the vertical resolution of raw lidar data (initial vertical resolution); k is the number of data points on either side of the central point N_j; $n = 2k + 1$ is the sliding average window size, i.e. the number of raw lidar data points determining the sliding average window length or data resolution after averaging (Otnes and Enochson, 1978). The weighting coefficients of the raw data points in Eq. (A3) are the same and equal to $1/(2k + 1)$. The vertical resolution of the averaged data series $\{\overline{N}_j\}$ is $\Delta\overline{z} = n\Delta z = (2k+1)\Delta z$. As the variance decreases by n times, the absolute uncertainty $\Delta\overline{N}(z)$ of averaged data decreases by $\sqrt{n}$ times. Therefore, for the absolute uncertainty of temperature retrieval from the averaged lidar data (photocounts) $\overline{N}_{\mathrm{H}}$ and $\overline{N}_{\mathrm{L}}$ we have

$$\Delta\overline{T} = \frac{\Delta T}{\sqrt{n}} = \left|\frac{dT}{dQ}\right| \frac{Q}{\sqrt{n}} \sqrt{\frac{1}{\overline{N}_{\mathrm{H}}} + \frac{1}{\overline{N}_{\mathrm{L}}}}, \tag{A5}$$

where $Q = \overline{N}_{\mathrm{L}} / \overline{N}_{\mathrm{H}}$. Hence, the confidence interval of the retrieved temperature profile is $[T - \Delta\overline{T}; T + \Delta\overline{T}]$, and the relative uncertainty is given by

$$\left(\frac{\overline{\Delta T}}{T}\right) = \left|\frac{dT}{dQ}\right| \frac{Q}{T\sqrt{n}} \sqrt{\frac{1}{\overline{N}_{\mathrm{H}}} + \frac{1}{\overline{N}_{\mathrm{L}}}}. \tag{A6}$$

In some cases, the second-order averaging of raw data (or/and their ratio) is required and more preferable than the first-order one (see, e.g., El'nikov et al., 2000). In such cases, the double-averaged data $\overline{\overline{N}}(z)$ and their variance $\overline{\overline{\mathrm{Var}}}(z)$ are related to the corresponding single-averaged data $\overline{N}(z)$, and variances $\overline{\mathrm{Var}}(z)$ and $\mathrm{Var}(z)$ as follows

$$\overline{\overline{N}}_j(z) = \frac{1}{2l+1} \sum_{i=-l}^{l} \overline{N}_{j+i} = \frac{1}{m} \sum_{i=-k}^{k} \overline{N}(z + i\Delta z), \tag{A7}$$

$$\overline{\overline{\mathrm{Var}}}(z) = \overline{\mathrm{Var}}(z) / m = \mathrm{Var}(z) / (n\,m), \tag{A8}$$

where l is the number of the single-averaged data points on either side of the central point $\overline{N}_j$; $m = 2l + 1$ is the sliding average window size. The confidence interval of a retrieved temperature profile is $[T - \Delta\overline{\overline{T}}; T + \Delta\overline{\overline{T}}]$, where $\Delta\overline{\overline{T}} = \Delta T / \sqrt{n\,m}$. There are two ways to average previously averaged PRR lidar data. The first way is to average the ratio $Q = \overline{N}_{\mathrm{L}} / \overline{N}_{\mathrm{H}}$ of the single-averaged data $\overline{N}_{\mathrm{H}}$ and $\overline{N}_{\mathrm{L}}$. In this case, the absolute and relative uncertainties of temperature retrieval from the averaged ratio $Q_{\mathrm{I}} = \overline{Q} = \overline{\overline{N}_{\mathrm{L}} / \overline{N}_{\mathrm{H}}}$ are given by

$$\Delta\overline{\overline{T}} = \left|\frac{dT}{dQ_{\mathrm{I}}}\right| \frac{Q_{\mathrm{I}}}{\sqrt{n\,m}} \sqrt{\frac{1}{\overline{N}_{\mathrm{H}}} + \frac{1}{\overline{N}_{\mathrm{L}}}}, \tag{A9}$$

$$\left(\overline{\overline{\frac{\Delta T}{T}}}\right) = \left|\frac{dT}{dQ_{\mathrm{I}}}\right| \frac{Q_{\mathrm{I}}}{T\sqrt{n\,m}} \sqrt{\frac{1}{\overline{N}_{\mathrm{H}}} + \frac{1}{\overline{N}_{\mathrm{L}}}}. \tag{A10}$$

The second way is to average the single-averaged data $\overline{N}_{\mathrm{H}}$ and $\overline{N}_{\mathrm{L}}$. The absolute and relative uncertainties of temperature retrieval from the double-averaged lidar data $\overline{\overline{N}}_{\mathrm{H}}$ and $\overline{\overline{N}}_{\mathrm{L}}$ (and for $Q_{\mathrm{II}} = \overline{\overline{N}}_{\mathrm{L}} \big/ \overline{\overline{N}}_{\mathrm{H}}$) are determined by

$$\Delta\overline{\overline{T}} = \left|\frac{dT}{dQ_{\mathrm{II}}}\right| \frac{Q_{\mathrm{II}}}{\sqrt{n\,m}} \sqrt{\frac{1}{\overline{\overline{N}}_{\mathrm{H}}} + \frac{1}{\overline{\overline{N}}_{\mathrm{L}}}}, \tag{A11}$$

$$\left(\overline{\overline{\frac{\Delta T}{T}}}\right) = \left|\frac{dT}{dQ_{\mathrm{II}}}\right| \frac{Q_{\mathrm{II}}}{T\sqrt{n\,m}} \sqrt{\frac{1}{\overline{\overline{N}}_{\mathrm{H}}} + \frac{1}{\overline{\overline{N}}_{\mathrm{L}}}}. \tag{A12}$$

The vertical resolution of the double-averaged data series $\{\overline{\overline{N}}_j\}$ and for both ways of the second-order averaging becomes

$$\Delta\overline{\overline{z}} = p\Delta z = [2(k+l)+1]\Delta z. \tag{A13}$$

If the window size n (and/or m) varies with altitude z, both the uncertainties should be estimated separately for each altitude interval where n = const (and/or m = const). To determine the weighting coefficients of the raw data points in Eq. (A7), it is necessary to consider three possible simple cases of the second-order averaging.

(1) Let $k > l$ ($n > m$), i.e. the sliding average window size for the first-order averaging is larger than that for the second-order one. Then

$$\overline{\overline{N}}_j = \frac{1}{(2l+1)(2k+1)}\left\{(2l+1)\left[N_j + \sum_{i=1}^{k-l}\left(N_{j-i} + N_{j+i}\right)\right] + \sum_{i=k-l+1}^{k+l}(k+l+1-i)\left(N_{j-i} + N_{j+i}\right)\right\}. \tag{A14}$$

The weighting coefficients can be determined from Eq. (A14) of the following form

$$\overline{\overline{N}}_j = \frac{1}{2k+1}\left[N_j + \sum_{i=1}^{k-l}\left(N_{j-i} + N_{j+i}\right)\right] + \sum_{i=k-l+1}^{k+l}\frac{k+l+1-i}{(2l+1)(2k+1)}\left(N_{j-i} + N_{j+i}\right). \tag{A15}$$

(2) Let $l > k$ ($m > n$), i.e. the window size for the second-order averaging is larger than that for the first-order one. Then

$$\overline{\overline{N}}_j = \frac{1}{(2k+1)(2l+1)}\left\{(2k+1)\left[N_j + \sum_{i=1}^{l-k}\left(N_{j-i}+N_{j+i}\right)\right] + \sum_{i=l-k+1}^{l+k}(l+k+1-i)\left(N_{j-i}+N_{j+i}\right)\right\}. \tag{A16}$$

The corresponding weighting coefficients are determined similar to case (1).

(3) Let $l = k$ ($m = n$), i.e. the window size for the second-order averaging is equal to that for the first-order one. Then

$$\overline{\overline{N}}_j = \frac{1}{(2k+1)^2}\left\{(2k+1)N_j + \sum_{i=1}^{2k}(2k+1-i)\left(N_{j-i}+N_{j+i}\right)\right\}. \tag{A17}$$

The weighting coefficients are determined similar to cases (1) and (2). The vertical resolution of the double-averaged data series $\{\overline{\overline{N}}_j\}$ in case (3) is $\Delta\overline{\overline{z}} = p\Delta z = (4k+1)\Delta z$ (El'nikov et al., 2000).

Appendix A0: Linear calibration function

As we applied the first way of the second-order averaging of the IMCES lidar raw data (see Appendix A and Sect. 4.1), we use Eqs. (A9) and (A10) to derive the absolute and relative uncertainties in an analytical form. In case of the first-order averaging of lidar raw data, one can use Eqs. (A5) and (A6), respectively.

In order to obtain both the uncertainties for the linear calibration function, let us differentiate the temperature retrieval function derived from Eq. (10), i.e. (see Sect. 2)

$$T = \frac{B_0}{\ln Q - A_0}. \tag{A18}$$

The first-order derivative of the function is

$$\frac{dT}{dQ} = -\frac{B_0}{Q(\ln Q - A_0)^2}. \tag{A19}$$

Substituting Eq. (A19) into Eq. (A9), for the absolute uncertainty we get

$$\Delta\overline{\overline{T}} = \frac{|B_0|}{(\ln Q_1 - A_0)^2\sqrt{nm}}\sqrt{\frac{1}{\overline{\overline{N}}_{\mathrm{H}}} + \frac{1}{\overline{\overline{N}}_{\mathrm{L}}}}. \tag{A20}$$

One can rewrite Eq. (A20) in more simple form by substituting the expression $\ln Q - A_0 = B_0/T$ derived from Eq. (A18)

$$\Delta\overline{\overline{T}} = \frac{T^2}{|B_0|\sqrt{nm}}\sqrt{\frac{1}{\overline{\overline{N}}_{\mathrm{H}}} + \frac{1}{\overline{\overline{N}}_{\mathrm{L}}}}. \tag{A21}$$

Consequently, substituting Eq. (A19) into Eq. (A10), for the relative uncertainty we have

$$\left(\frac{\overline{\overline{\Delta T}}}{T}\right)=\frac{1}{\left|\ln Q_{\mathrm{I}}-A_0\right|\sqrt{nm}}\sqrt{\frac{1}{\overline{\overline{N}}_{\mathrm{H}}}+\frac{1}{\overline{\overline{N}}_{\mathrm{L}}}}=\frac{T}{\left|B_0\right|\sqrt{nm}}\sqrt{\frac{1}{\overline{\overline{N}}_{\mathrm{H}}}+\frac{1}{\overline{\overline{N}}_{\mathrm{L}}}}\,. \tag{A22}$$

Appendix A1: Calibration function quadratic in *x* = 1/*T*

The temperature retrieval function derived from Eq. (12) is written as (see Sect. 2)

$$T=\frac{2C_1}{-B_1\pm\sqrt{B_1^2+4C_1\left(\ln Q-A_1\right)}}\,. \tag{A23}$$

The sign "+" instead of "±" should be chosen in the denominator of Eq. (A23), if $Q = N_{\mathrm{L}}/N_{\mathrm{H}}$. When applying Eq. (A23) for temperature retrievals, one should take into account the constraint coming from the square root. Namely, the expression under the square root should be nonnegative, i.e. $B_1^2+4C_1\left[\ln Q(z)-A_1\right]\geq 0$ or $\ln Q(z)\leq (B_1^2/4C_1)-A_1$. Hence, Eq. (A23) can retrieve the temperature profile T only at altitudes z where this condition holds.

The first-order derivative of the function is

$$\frac{dT}{dQ}=\frac{-4C_1^2\left[-B_1+\sqrt{B_1^2+4C_1\left(\ln Q-A_1\right)}\;\right]^{-2}}{Q\sqrt{B_1^2+4C_1\left(\ln Q-A_1\right)}}\,. \tag{A24}$$

It is clear that the expressions for both absolute and relative uncertainties will be cumbersome and poorly adapted for use after substitution of this derivative in Eqs. (A9) and (A10). However, Eq. (A24) can be put in a more convenient form by substituting the expressions which follow from Eq. (A23)

$$\begin{aligned}&-B_1+\sqrt{B_1^2+4C_1\left(\ln Q-A_1\right)}=\frac{2C_1}{T}\,,\\&\sqrt{B_1^2+4C_1\left(\ln Q-A_1\right)}=\frac{2C_1}{T}+B_1\,.\end{aligned} \tag{A25}$$

After substitution of Eqs. (A25) into Eq. (A24), we can write instead of Eq. (A24)

$$\frac{dT}{dQ}=\frac{-T^3}{Q(2C_1+B_1T)}\,. \tag{A26}$$

Substituting Eq. (A26) into Eqs. (A9) and (A10), we obtain correspondingly for the absolute and relative uncertainties

$$\Delta\overline{\overline{T}} = \frac{T^3}{\left|2C_1 + B_1 T\right|\sqrt{nm}}\sqrt{\frac{1}{\overline{\overline{N}}_{\mathrm{H}}} + \frac{1}{\overline{\overline{N}}_{\mathrm{L}}}}\,, \tag{A27}$$

$$\left(\frac{\overline{\overline{\Delta T}}}{T}\right) = \frac{T^2}{\left|2C_1 + B_1 T\right|\sqrt{nm}}\sqrt{\frac{1}{\overline{\overline{N}}_{\mathrm{H}}} + \frac{1}{\overline{\overline{N}}_{\mathrm{L}}}}\,. \tag{A28}$$

Appendix A2: Calibration function hyperbolic in *x* = 1/*T*

The temperature retrieval function in the general form derived from Eq. (14) represents (see Sect. 2)

$$T = \frac{2B_2}{(\ln Q - A_2) \pm \sqrt{(\ln Q - A_2)^2 - 4B_2C_2}}\,. \tag{A29}$$

For the case of $Q = N_{\mathrm{L}}/N_{\mathrm{H}}$, the sign “+” instead of “±” should also be chosen in the denominator of Eq. (A29). Note that Eq. (A29) can retrieve the temperature T only at altitudes z where the following condition holds: $[\ln Q(z) - A_2]^2 - 4B_2C_2 \geq 0$ or $\ln Q(z) \geq A_2 + 2\sqrt{B_2C_2}$ (with $B_2C_2 \geq 0$).

The derivative of the temperature retrieval function is

$$\frac{dT}{dQ} = \frac{2B_2}{Q\left[(\ln Q - A_2) + \sqrt{(\ln Q - A_2)^2 - 4B_2C_2}\right]^2} \times \left[1 + \frac{\ln Q - A_2}{\sqrt{(\ln Q - A_2)^2 - 4B_2C_2}}\right]. \tag{A30}$$

Equation (A30) can be put in a more convenient form by substituting the expressions which follow from Eqs. (A29) and (14), respectively

$$\begin{aligned} &(\ln Q - A_2) + \sqrt{(\ln Q - A_2)^2 - 4B_2C_2} = 2B_2/T\,, \\ &\ln Q - A_2 = B_2/T + C_2 T\,. \end{aligned} \tag{A31}$$

After substitution of Eqs. (A31) into Eq. (A30), we get for the derivative

$$\frac{dT}{dQ} = \frac{T^2}{Q\left(B_2 - C_2T^2\right)}\,. \tag{A32}$$

Then substituting Eq. (A32) into Eqs. (A9) and (A10), we obtain for both the uncertainties

$$\Delta\overline{\overline{T}} = \frac{T^2}{\left|B_2 - C_2 T^2\right|\sqrt{nm}}\sqrt{\frac{1}{\overline{\overline{N}}_{\mathrm{H}}} + \frac{1}{\overline{\overline{N}}_{\mathrm{L}}}}\,, \tag{A33}$$

$$\left(\frac{\overline{\overline{\Delta T}}}{T}\right) = \frac{T}{\left|B_2 - C_2 T^2\right|\sqrt{nm}}\sqrt{\frac{1}{\overline{\overline{N}}_{\mathrm{H}}} + \frac{1}{\overline{\overline{N}}_{\mathrm{L}}}}\,. \tag{A34}$$

Appendix A3: Calibration function quadratic in *y* = ln*Q*

The first-order derivative of the temperature retrieval function, obtained from Eq. (16) (see Sect. 2)

$$T = \frac{C_3}{(\ln Q)^2 + B_3 \ln Q + A_3}, \tag{A35}$$

is simply expressed as

$$\frac{dT}{dQ} = \frac{-C_3(2\ln Q + B_3)}{Q\left[(\ln Q)^2 + B_3 \ln Q + A_3\right]^2}\,. \tag{A36}$$

Substituting Eq. (A36) into Eq. (A9), for the absolute uncertainty we get

$$\Delta\overline{\overline{T}} = \frac{\left|C_3(2\ln Q_{\mathrm{I}} + B_3)\right|}{\left[(\ln Q_{\mathrm{I}})^2 + B_3 \ln Q_{\mathrm{I}} + A_3\right]^2\sqrt{nm}}\sqrt{\frac{1}{\overline{\overline{N}}_{\mathrm{H}}} + \frac{1}{\overline{\overline{N}}_{\mathrm{L}}}}\,. \tag{A37}$$

Using the expression derived from Eq. (A35), i.e.

$$(\ln Q)^2 + B_3 \ln Q + A_3 = C_3/T\,, \tag{A38}$$

for the relative uncertainty we obtain

$$\left(\frac{\overline{\overline{\Delta T}}}{T}\right) = \left|\frac{2\ln Q_{\mathrm{I}} + B_3}{(\ln Q_{\mathrm{I}})^2 + B_3 \ln Q_{\mathrm{I}} + A_3}\right|\frac{1}{\sqrt{nm}}\sqrt{\frac{1}{\overline{\overline{N}}_{\mathrm{H}}} + \frac{1}{\overline{\overline{N}}_{\mathrm{L}}}}\,. \tag{A39}$$

In order to estimate both the uncertainties, one can also use Eqs. (A37) and (A39) in a more simple form. Substituting Eq. (A38) in Eqs (A37) and (A39), we obtain the following equations containing both lnQ_{I} and retrieved temperature T:

$$\Delta\overline{\overline{T}} = \left|\frac{2\ln Q_{\mathrm{I}} + B_3}{C_3}\right|\frac{T^2}{\sqrt{nm}}\sqrt{\frac{1}{\overline{\overline{N}}_{\mathrm{H}}} + \frac{1}{\overline{\overline{N}}_{\mathrm{L}}}}\,, \tag{A40}$$

$$\left(\frac{\overline{\overline{\Delta T}}}{T}\right) = \left|\frac{2\ln Q_{\mathrm{I}} + B_3}{C_3}\right| \frac{T}{\sqrt{nm}} \sqrt{\frac{1}{\overline{\overline{N}}_{\mathrm{H}}} + \frac{1}{\overline{\overline{N}}_{\mathrm{L}}}} \,. \tag{A41}$$

Appendix A4: Calibration function hyperbolic in $y = \ln Q$

Tropospheric temperature profiles are mentioned in Sect. 2 can also be retrieved via the function

$$T = \frac{\ln Q}{B_4 (\ln Q)^2 + A_4 \ln Q + C_4} \,, \tag{A42}$$

which first-order derivative is defined as

$$\frac{dT}{dQ} = \frac{C_4 - B_4 (\ln Q)^2}{Q\left[B_4 (\ln Q)^2 + A_4 \ln Q + C_4\right]^2} \,. \tag{A43}$$

Substituting Eq. (A43) in Eq. (A9), we obtain the absolute uncertainty containing only ln$Q$

$$\overline{\overline{\Delta T}} = \frac{\left|C_4 - B_4 (\ln Q_{\mathrm{I}})^2\right|}{\left[B_4 (\ln Q_{\mathrm{I}})^2 + A_4 \ln Q_{\mathrm{I}} + C_4\right]^2 \sqrt{nm}} \sqrt{\frac{1}{\overline{\overline{N}}_{\mathrm{H}}} + \frac{1}{\overline{\overline{N}}_{\mathrm{L}}}} \,. \tag{A44}$$

Using the expression derived from Eq. (A42), i.e.

$$B_4 (\ln Q)^2 + A_4 \ln Q + C_4 = (\ln Q)/T \,, \tag{A45}$$

for the relative uncertainty we get

$$\left(\frac{\overline{\overline{\Delta T}}}{T}\right) = \left|\frac{C_4 - B_4 (\ln Q_{\mathrm{I}})^2}{B_4 (\ln Q_{\mathrm{I}})^3 + A_4 (\ln Q_{\mathrm{I}})^2 + C_4 \ln Q_{\mathrm{I}}}\right| \frac{1}{\sqrt{nm}} \sqrt{\frac{1}{\overline{\overline{N}}_{\mathrm{H}}} + \frac{1}{\overline{\overline{N}}_{\mathrm{L}}}}. \tag{A46}$$

Similarly, using Eq. (A45), one can rewrite Eqs. (A44) and (A46) in a practically useful form:

$$\overline{\overline{\Delta T}} = \left|\frac{C_4}{(\ln Q_{\mathrm{I}})^2} - B_4\right| \frac{T^2}{\sqrt{nm}} \sqrt{\frac{1}{\overline{\overline{N}}_{\mathrm{H}}} + \frac{1}{\overline{\overline{N}}_{\mathrm{L}}}}, \tag{A47}$$

$$\left(\frac{\overline{\overline{\Delta T}}}{T}\right) = \left|\frac{C_4}{(\ln Q_{\mathrm{I}})^2} - B_4\right| \frac{T}{\sqrt{nm}} \sqrt{\frac{1}{\overline{\overline{N}}_{\mathrm{H}}} + \frac{1}{\overline{\overline{N}}_{\mathrm{L}}}}. \tag{A48}$$

Acknowledgements

We thank Dr. S. M. Bobrovnikov for helpful discussions. This study was conducted in the framework of the Federal Targeted Programme «R&D in Priority Fields of S&T Complex of Russia for 2014–2020» in the Priority Field "Rational use of natural resources" (contract No. 14.607.21.0030, unique identifier ASR RFMEFI60714X0030).

References

Achtert, P., Khaplanov, M., Khosrawi, F., and Gumbel, J.: Pure rotational-Raman channels of the Esrange lidar for temperature and particle extinction measurements in the troposphere and lower stratosphere, Atmos. Meas. Tech., 6, 91–98, 2013.

Alpers, M., Eixmann, R., Fricke-Begemann, C., Gerding, M., and Höffner, J.: Temperature lidar measurements from 1 to 105 km altitude using resonance, Rayleigh, and rotational Raman scattering, Atmos. Chem. Phys., 4, 793–800, 2004.

Ansmann, A., Arshinov Y., Bobrovnikov, S. M., Mattis, I., Serikov, I. B., and Wandinger, U.: Double-grating monochromator for a pure rotational Raman lidar, Proc. SPIE, 3583, 491–497, doi:10.1117/12.337058, 1999.

Arshinov, Y. F., Bobrovnikov, S. M., Zuev, V. E., and Mitev, V. M.: Atmospheric temperature measurements using a pure rotational Raman lidar, Appl. Optics, 22, 2984–2990, 1983.

Behrendt A. and Reichardt, J.: Atmospheric temperature profiling in the presence of clouds with a pure rotational Raman lidar by use of an interference-filter-based polychromator, Appl. Optics, 39, 1372–1378, 2000.

Behrendt, A., Nakamura, T., Onishi, M., Baumgart, R., and Tsuda, T.: Combined Raman lidar for the measurement of atmospheric temperature, water vapor, particle extinction coefficient, and particle backscatter coefficient, Appl. Optics, 41, 7657–7666, 2002.

Behrendt, A.: Temperature measurements with lidar, in: Lidar: Range-Resolved Optical Remote Sensing of the Atmosphere, edited by: Weitkamp, C., Springer, New York, 2005.

Behrendt, A., Wulfmeyer, V., Hammann, E., Muppa, S. K., and Pal, S.: Profiles of second- to fourth-order moments of turbulent temperature fluctuations in the convective boundary layer: first measurements with rotational Raman lidar, Atmos. Chem. Phys, 15, 5485–5500, 2015.

Chen, S., Qiu, Z., Zhang, Y., Chen, H., and Wang, Y.: A pure rotational Raman lidar using double-grating monochromator for temperature profile detection, J. Quant. Spectr. Rad. Transfer, 112, 304–309, 2011.

Cooney, J.: Measurement of atmospheric temperature profiles by Raman backscatter, J. Appl. Meteorol., 11, 108–112, 1972.

Di Girolamo, P., Marchese, R., Whiteman, D. N., and Demoz, B. B.: Rotational Raman Lidar measurements of atmospheric temperature in the UV, Geophys. Res. Lett., 31, L01106, doi:10.1029/2003GL018342, 2004.

El'nikov, A. V., Zuev, V. V., and Bondarenko, S. L.: Retrieving the profiles of stratospheric ozone from lidar sensing data, Atm. and Oceanic Optics, 13, 1029–1034, 2000.

Gerasimov, V. V., Zuev, V. V., Pravdin, V. L., Nakhtigalova, D. P., and Pavlinskiy A. V.: Collision broadening effect upon tropospheric temperature calibration functions for pure rotational Raman lidars, Proc. SPIE, 9680, 96804F, doi: 10.1117/12.2205832, 2015.

Gerasimov, V. V. and Zuev, V. V.: Analytical calibration functions for the pure rotational Raman lidar technique, Opt. Express, 24, 5136–5151, 2016.

Ginzburg, V. L.: Line width in the spectrum of scattered light, Sov. Phys. Usp., 15, 114–120, 1972.

Hammann, E., Behrendt, A., Le Mounier, F., and Wulfmeyer, V.: Temperature profiling of the atmospheric boundary layer with rotational Raman lidar during the HD(CP)^2 Observational Prototype Experiment, Atmos. Chem. Phys., 15, 2867–2881, 2015.

Hammann, E. and Behrendt, A.: Parametrization of optimum filter passbands for rotational Raman temperature measurements, Opt. Express, 23, 30767–30782, 2015.

Ivanova, I. D., Gurdev, L. L., and Mitev, V. M.: Lidar technique for simultaneous temperature and pressure measurement based on rotation Raman scattering, J. Mod. Opt., 40, 367–371, 1993.

Jia, J. and Yi, F.: Atmospheric temperature measurements at altitudes of 5–30 km with a double-grating-based pure rotational Raman lidar, Appl. Optics, 53, 5330–5343, 2014.

Kim, D., Cha, H., Lee, J., and Bobronikov, S.: Pure rotational Raman lidar for atmospheric temperature measurements, J. Korean Phys. Soc., 39, 838–841, 2001.

Lee III, R. B.: Tropospheric temperature measurements using a rotational Raman lidar, Ph.D. dissertation, Hampton University, Hampton, Virginia, 112 pp., 2013, available at: http://pqdtopen.proquest.com/doc/1437652821.html?FMT=AI.

Li, Y.-J., Song, S.-L., Li, F.-Q., Cheng X.-W., Chen, Z.-W., Liu, L.-M., Yang, Y., and Gong, S.-S.: High-precision measurements of lower atmospheric temperature based on pure rotational Raman lidar, Chinese J. Geophys., 58, 2294–2305, 2015.

Measures, R. M.: Laser remote sensing. Fundamentals and applications, John Wiley & Sons, New York, 1984.

Nedeljkovic, D., Hauchecorne, A., and Chanin, M.-L.: Rotational Raman lidar to measure the atmospheric temperature from ground to 30km, IEEE T. Geosci. Remote, 31, 90–101, 1993.

Newsom, R. K., Sivaraman, C., and McFarlane, S. A.: Raman lidar profiles–temperature (RLPROFTEMP) value-added product: available at: https://www.arm.gov/publications/tech_reports/doe-sc-arm-tr-120.pdf, 2012.

Newsom, R. K., Turner, D. D., and Goldsmith, J. E. M.: Long-term evaluation of temperature profiles measured by an operational Raman lidar, J. Atmos. Oceanic Technol., 30, 1616–1634, 2013.

Otnes, R. K. and Enochson, L.: Applied Time Series Analysis. Vol. 1. Basic Techniques, John Wiley & Sons, New York, 1978.

Radlach, M., Behrendt, A., and Wulfmeyer, V.: Scanning rotational Raman lidar at 355 nm for the measurement of tropospheric temperature fields, Atmos. Chem. Phys., 8, 159–169, 2008.

Radlach, M.: A scanning eye-safe rotational Raman lidar in the ultraviolet for measurements of tropospheric temperature fields, Ph.D. dissertation, University of Hohenheim, Stuttgart, Germany, 117 pp., 2009, available at: https://opus.uni-hohenheim.de/volltexte/2009/345/pdf/Radlach_doctoral_thesis_engl_LINKS.pdf.

Penney, C. M., Peters St., R. L., and Lapp, M.: Absolute rotational Raman cross sections for N_2, O_2, and CO_2, J. Opt. Soc. Amer., 64, 712–716, 1974.

Wandinger, U.: Raman lidar, in: Lidar: Range-Resolved Optical Remote Sensing of the Atmosphere, edited by: Weitkamp, C., Springer, New York, 2005.

Wulfmeyer, V., Hardesty, R. M., Turner, D. D., Behrendt, A., Cadeddu, M. P., Di Girolamo, P., Schlüssel, P., Van Baelen, J., and Zus, F.: A review of the remote sensing of lower tropospheric thermodynamic profiles and its indispensable role for the understanding and the simulation of water and energy cycles. Rev. Geophys., 53, 819–895, 2015.

Table 1. Main technical parameters of the IMCES lidar transmitting, receiving, and data acquisition systems.

Transmitting system	
Laser	
Type	Unseeded frequency-tripled Nd:YAG
Model	Solar LS LQ529B
Wavelength	354.67 nm
Spectral line width	~ 1 cm^{-1}
Pulse repetition rate	20 Hz
Pulse energy	105 mJ
Pulse duration	13 ns
Beam divergence	0.3 mrad
Expansion factor	10
Receiving system	
Telescope	
Type	Prime-focus
Receiving mirror diameter	0.5 m
Focal length	1.5 m
Field of view	0.4 mrad
Optical fibers	
F0 input fiber diameter	0.55 mm (FG 550 UER)
F1 output fiber diameter	0.6 mm (FT 600 UMT)
FB intermediate fibers diameter	0.6 mm (FT 600 UMT)
F2 and F3 output fibers diameter	1.5 mm (FT 1.5 UMT)
Double-grating monochromator	
Lens L1, L2	
Diameter	130 mm
Focal length	300 mm
Diffraction gratings DG1, DG2	
Grooves / mm	2100
Diffraction order	2
Diffraction angle	48.151°

Data acquisition system	
Photomultiplier tubes PMT1–PMT3	Hamamatsu R7207-01
PMTs quantum efficiency	25%
Photon counter	PHCOUNT_4 (IMCES SB RAS)
Number of channels	4 (3 in use)
Counting rate	Up to 200 counts/s
Initial vertical resolution	24 m

Table 2. Spectral selection parameters of the DGM channels (central wavelength (CWL) and full width at half maximum (FWHM)).

DGM channel	CWL, nm	FWHM, nm/cm^{-1}
J_{low} (Stokes)	355.22	~0.22/17
J_{low} (anti-Stokes)	354.12	~0.22/17
J_{high} (Stokes)	356.03	~0.35/28
J_{high} (anti-Stokes)	353.32	~0.35/28

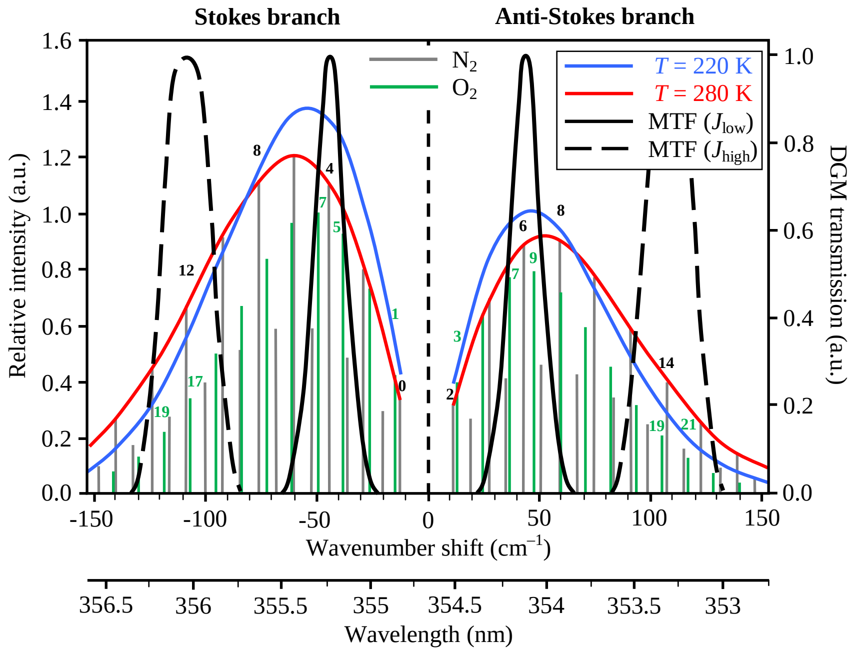

Figure 1. Equidistant PRR spectra of N_2 and O_2 linear molecules, schematic drawing of the IMCES lidar monochromator transmission functions (MTF) and envelopes of N_2 PRR spectrum at different temperatures. The red and blue envelopes correspond to the temperature of 280 and 220 K, respectively. The laser beam wavelength is 354.67 nm. The index over a spectral line denotes the rotational quantum number J of the initial state of the transition. The spectral line number and number J are the same for the Stokes branch. All PRR lines intensities are normalized to the intensity of N_2 PRR line with J = 6 of the anti-Stokes branch at T = 220 K.

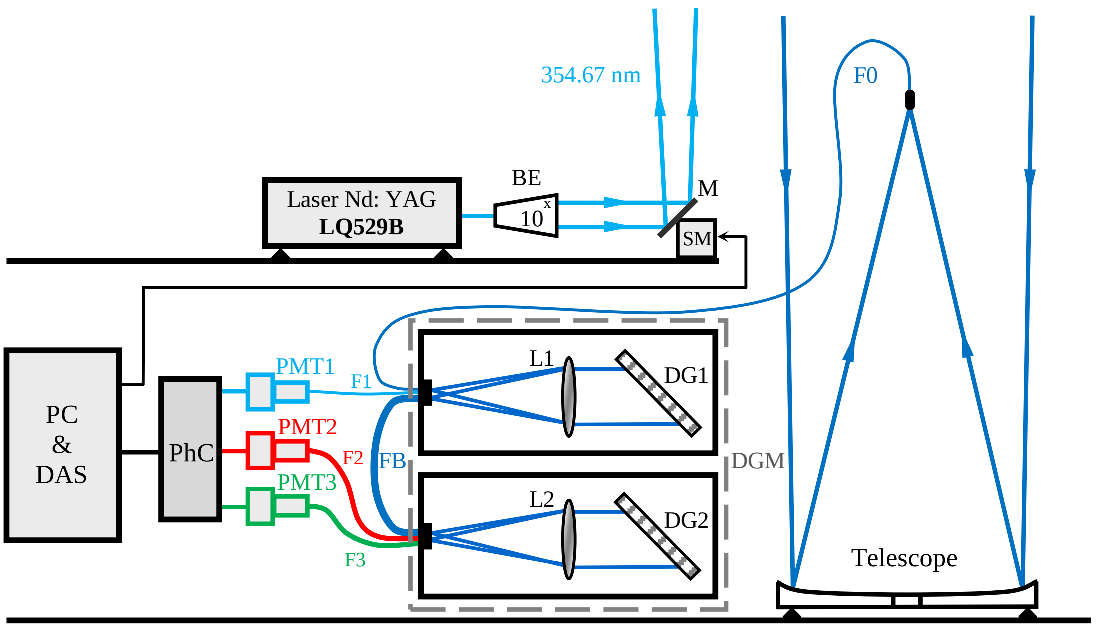

Figure 2. IMCES lidar optical layout (see also Table 1): PC&DAS, personal computer and data acquisition system; PhC, photon counter; PMT1–PMT3, photomultiplier tubes; F0–F3, optical fibers; FB, four fiber bundle, connecting two monochromator blocks; DGM, double-grating monochromator; L1 and L2, lenses; DG1 and DG2, diffraction gratings; BE, beam expander with expansion factor of 10; M, mirror; SM, stepping motor.

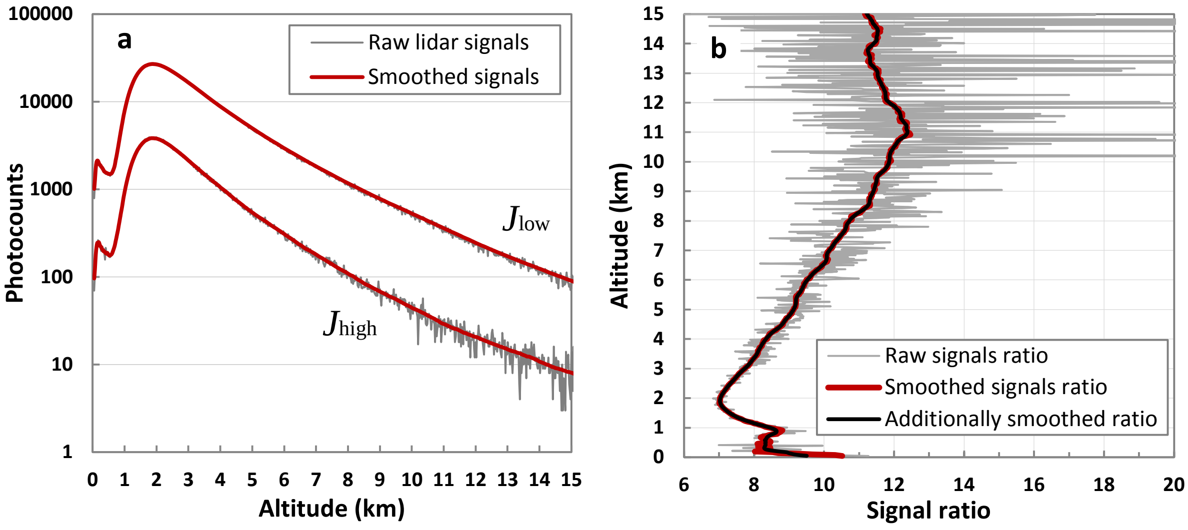

Figure 3. IMCES lidar data taken between 03:45 and 05:15 LT on 1 April 2015 (31 March, 21:45–23:15 UTC). **(a)** Raw photocounts N_L and N_H detected in the lidar channels with J_{low} and J_{high}, respectively, together with the single-averaged ones $\overline{N}_L$ and $\overline{N}_H$. **(b)** Raw photocounts ratio $Q = N_L/N_H$, single-averaged photocounts ratio $Q = \overline{N}_L \big/ \overline{N}_H$, and additionally averaged ratio $Q_I = \overline{Q} = \overline{\overline{N}_L \big/ \overline{N}_H}$.

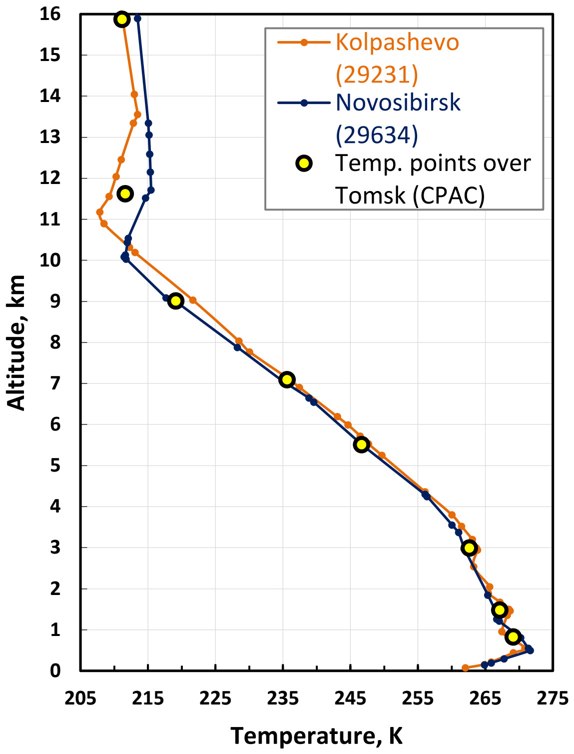

Figure 4. Temperature profiles from radiosondes launched on 1 April 2015 at 06:00 LT (00:00 UTC) in Novosibirsk (station 29634) and Kolpashevo (station 29231) as well as temperature points over Tomsk retrieved from constant pressure altitude charts (CPACs).

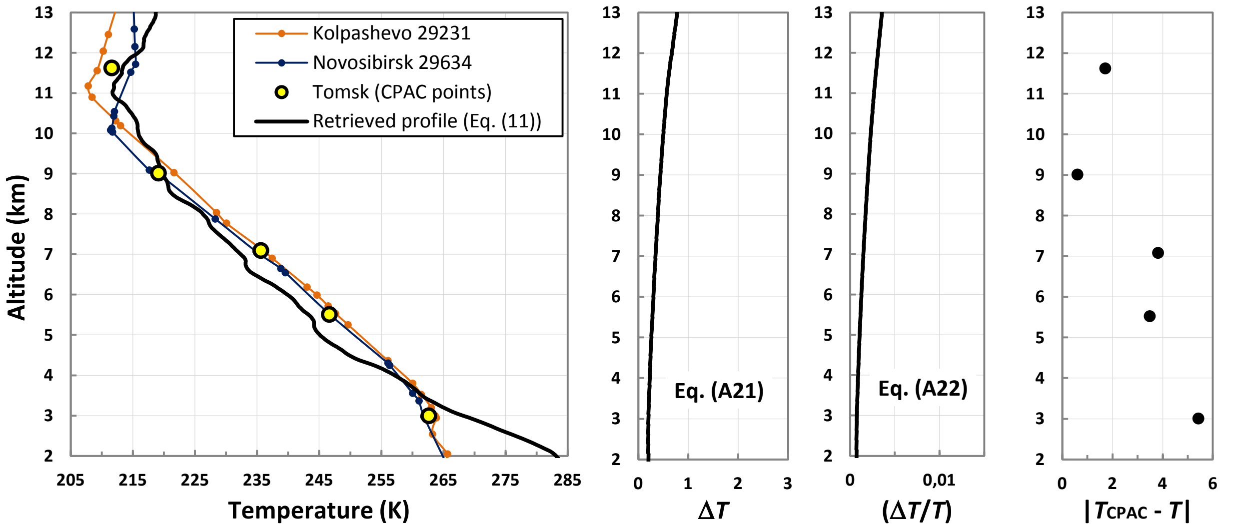

Figure 5. (1 April 2015) Temperature profile retrieved using the temperature retrieval function (Eq. 11) derived from the standard linear calibration function (Eq. 10, Arshinov et al., 1983). The absolute and relative uncertainties $\Delta T = \overline{\overline{\Delta T}}$ and $(\Delta T / T) = \overline{\overline{(\Delta T / T)}}$ are calculated by Eqs. (A21) and (A22), respectively. The values T_{CPAC} over Tomsk are retrieved from the 700, 500, 400, 300, and 200 hPa constant pressure altitude charts (CPACs). The radiosondes data from the nearest station in Novosibirsk and Kolpashevo are given for comparison.

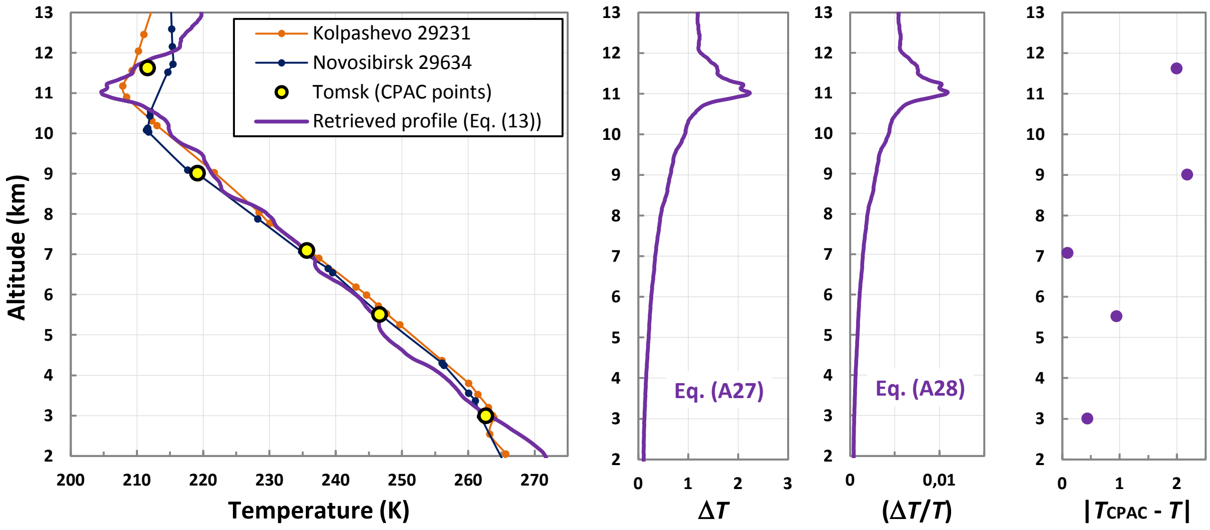

Figure 6. (1 April 2015) Temperature profile retrieved using the temperature retrieval function (Eq. 13) derived from the standard calibration function suggested by Behrendt and Reichardt (2000). The uncertainties ΔT and $(\Delta T/T)$ are calculated by Eqs. (A27) and (A28), respectively.

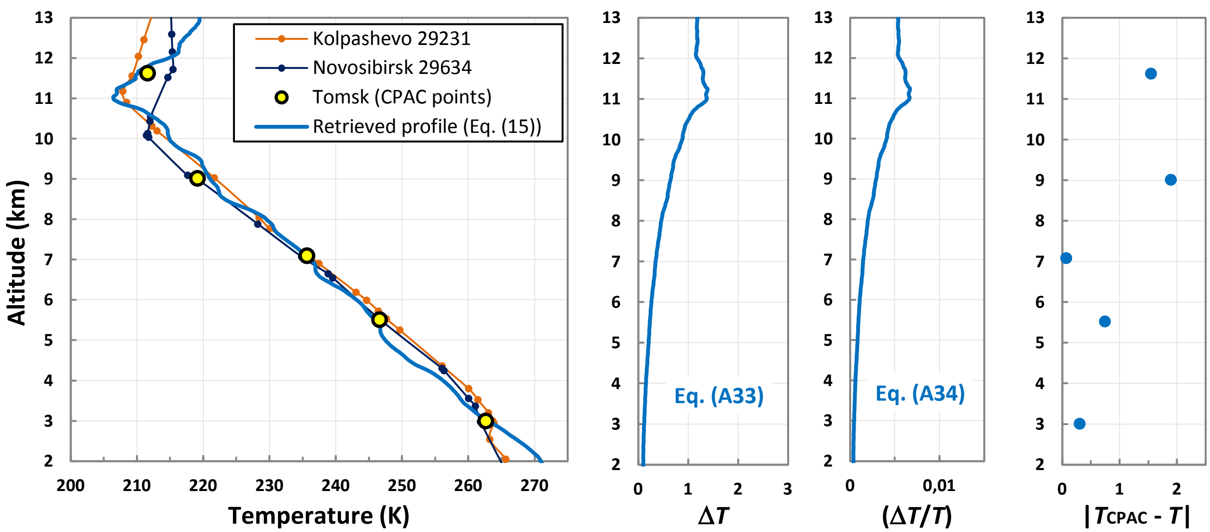

Figure 7. (1 April 2015) Temperature profile retrieved using the temperature retrieval function (Eq. 15) derived from the calibration function suggested by Gerasimov and Zuev (2016). The uncertainties ΔT and $(\Delta T/T)$ are calculated by Eqs. (A33) and (A34), respectively.

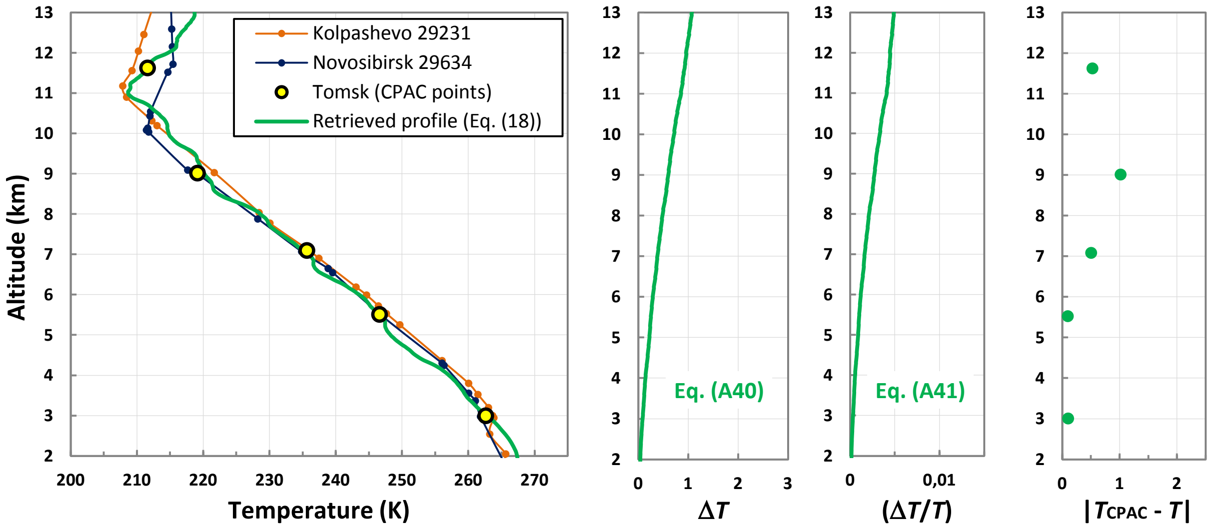

Figure 8. (1 April 2015) Temperature profile retrieved using the temperature retrieval function (Eq. 18) derived from the calibration function suggested by Lee III (2013). The uncertainties ΔT and $(\Delta T/T)$ are calculated by Eqs. (A40) and (A41), respectively.

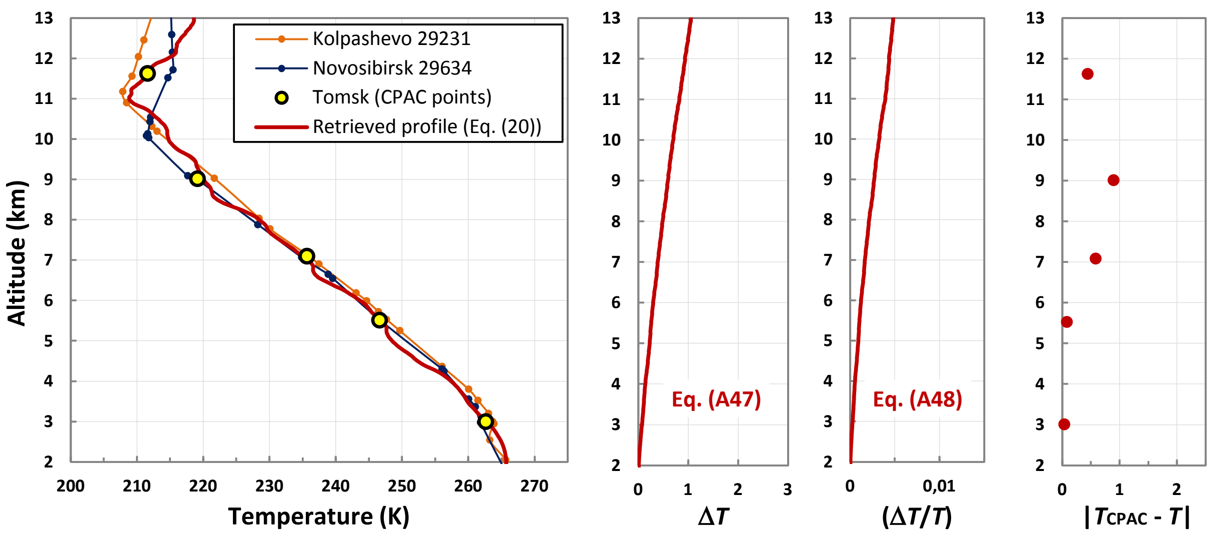

Figure 9. (1 April 2015) Temperature profile retrieved using the temperature retrieval function (Eq. 20) derived from the calibration function suggested by Gerasimov and Zuev (2016). The uncertainties ΔT and $(\Delta T/T)$ are calculated by Eqs. (A47) and (A48), respectively.

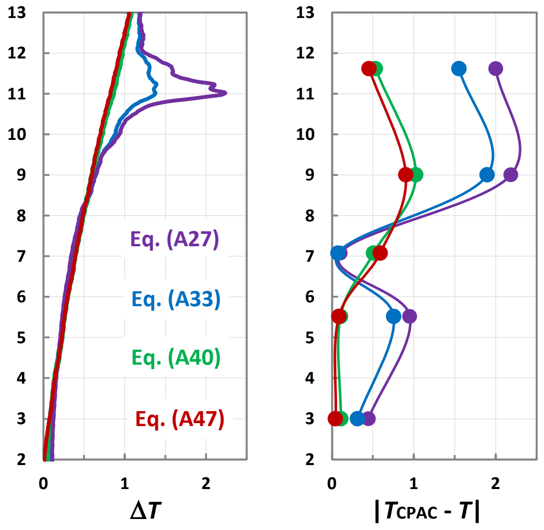

Figure 10. (1 April 2015) Comparative analysis of the absolute temperature uncertainties yielded by using Eqs. (A27), (A33), (A40), and (A47), and of the difference in modulus between temperature values retrieved from the CPACs and IMCES lidar data.

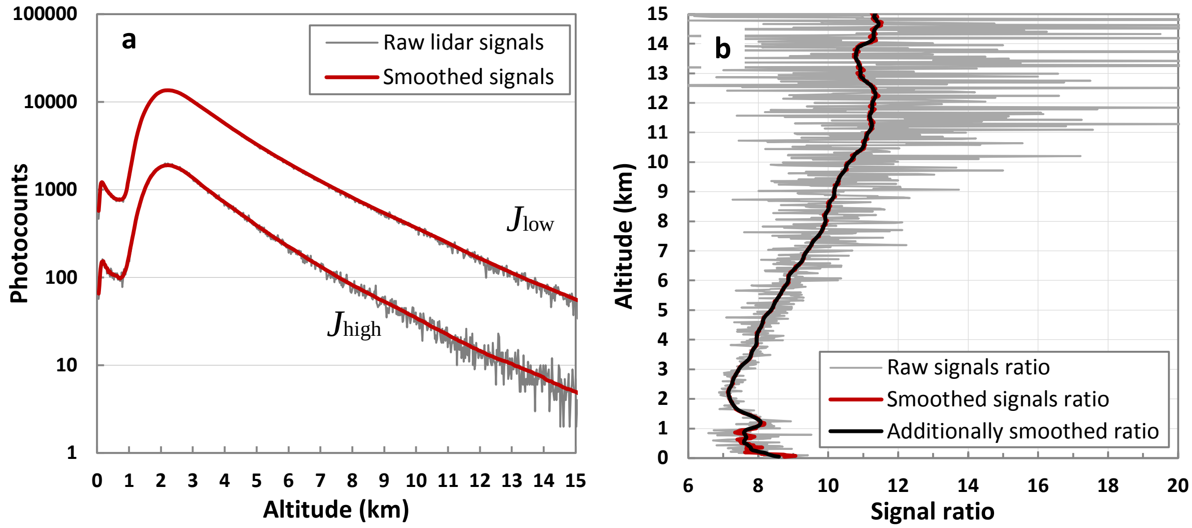

Figure 11. IMCES lidar data taken between 20:21 and 21:21 LT on 2 October 2014 (13:21–14:21 UTC). **(a)** Raw photocounts N_L and N_H detected in the lidar channels with J_{low} and J_{high}, respectively, together with the single-averaged ones $\overline{N}_L$ and $\overline{N}_H$. **(b)** Raw photocounts ratio $Q = N_L/N_H$, single-averaged photocounts ratio $Q = \overline{N}_L / \overline{N}_H$, and additionally averaged ratio $Q_I = \overline{Q} = \overline{\overline{N}_L / \overline{N}_H}$.

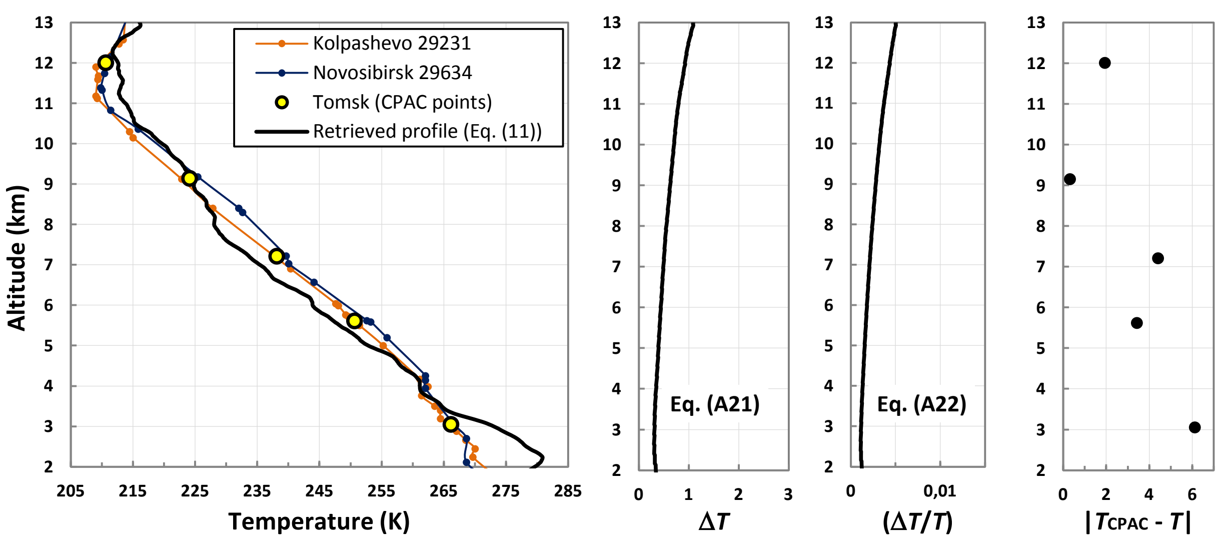

Figure 12. (2 October 2014) Temperature profile retrieved using Eq. (11). The absolute and relative uncertainties $\Delta T = \Delta\overline{\overline{T}}$ and $(\Delta T / T) = (\overline{\overline{\Delta T / T}})$ are calculated by Eqs. (A21) and (A22), respectively.

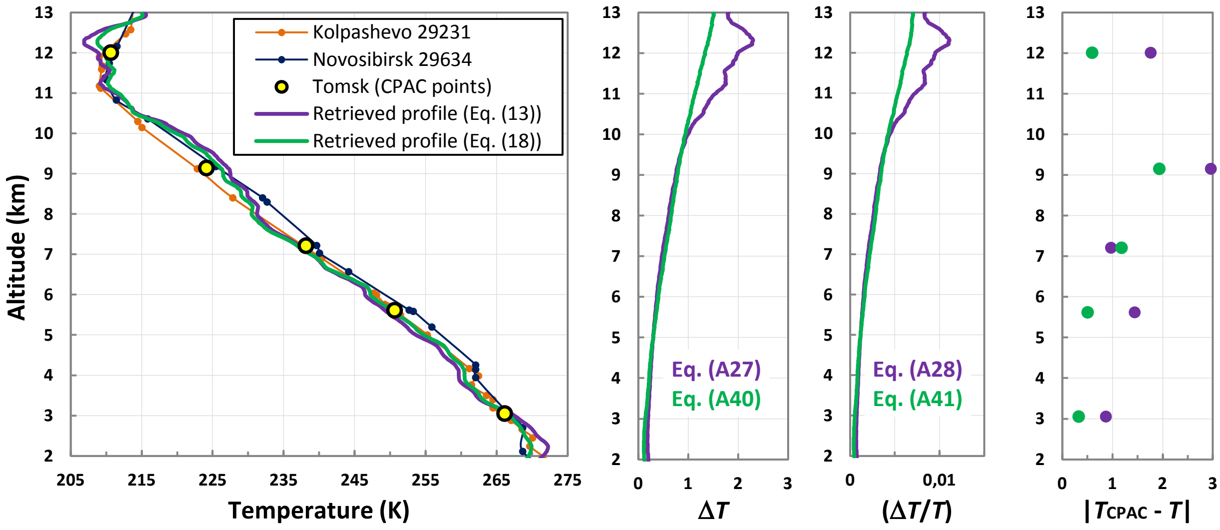

Figure 13. (2 October 2014) Temperature profiles retrieved using Eqs. (13) and (18).

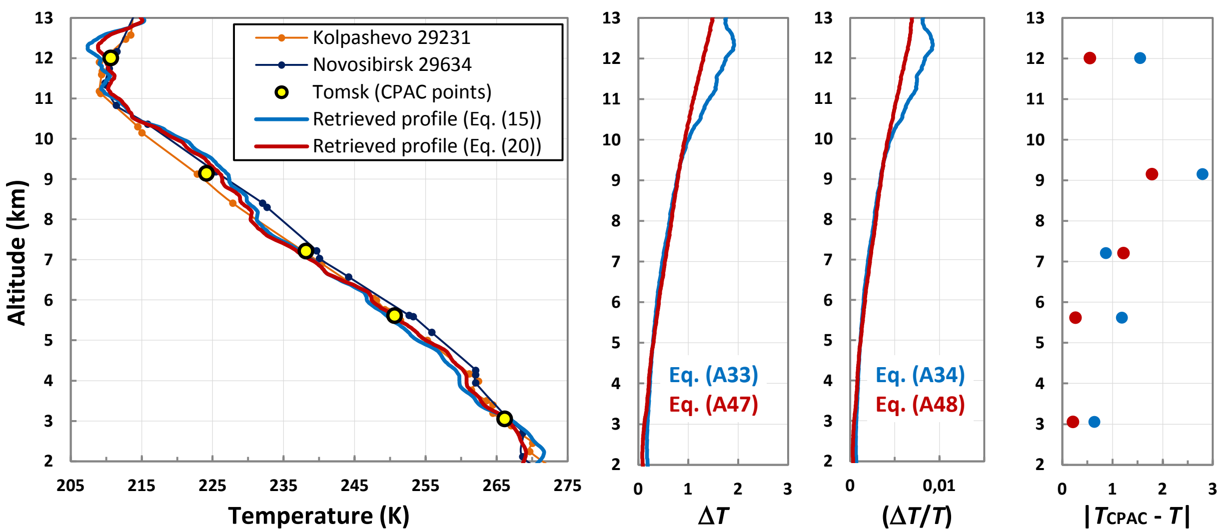

Figure 14. (2 October 2014) Temperature profiles retrieved using Eqs. (15) and (20).

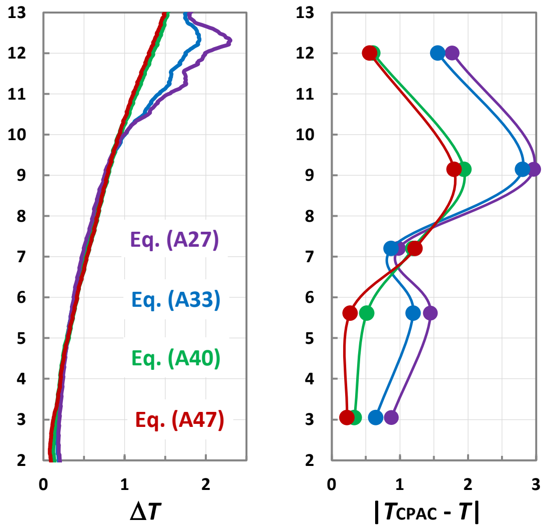

Figure 15. (2 October 2014) Comparative analysis of the absolute temperature uncertainties yielded by using Eqs. (A27), (A33), (A40), and (A47), and of the difference in modulus between temperature values retrieved from the CPACs and IMCES lidar data.